Manuscript prepared for Geosci. Model Dev.
with version 2.3 of the LaTeX class copernicus.cls.
Date: 7 September 2009

Formulation and numerical studies by the Dutch Atmospheric Large-Eddy Simulation (DALES)

Thijs Heus[1,6], Chiel C. van Heerwaarden[2], Harm J. J. Jonker[3], A. Pier Siebesma[1,3], Simon Axelsen[4], Kees van den Dries[2], Olivier Geoffroy[1], Arnold Moene[2], David Pino[5], Stephan R. de Roode[3], and Jordi Vilà-Guerau de Arellano[2]

[1]Royal Netherlands Meteorological Institute, De Bilt, the Netherlands
[2]Meteorology and Air Quality Section, Wageningen University, Wageningen, the Netherlands
[3]Dept. of Multi-Scale Physics, Delft University of Technology, Delft, the Netherlands
[4]Institute for Marine and Atmospheric Research Utrecht, Utrecht University, Utrecht, the Netherlands
[5]Applied Physics Department, Technical University of Catalonia, and Institute for Space Studies of Catalonia (IEEC/CSIC), Barcelona, Spain
[6]Max Planck Institute for Meteorology, Hamburg, Germany

Abstract. The current version of the Dutch Atmospheric Large-Eddy Simulation (DALES) model is presented. DALES is a large-eddy simulation model designed for process studies of the atmospheric boundary layer, including convective and stable boundary layers as well as cloudy boundary layers. In addition DALES can be used for studies of more specific cases, such as flow over sloped or heterogeneous terrain, and dispersion of inert and chemically active species. This paper contains an extensive description and evaluation of the DALES code and gives an overview of its applications and accomplishments in recent years.

1 TODO

1.1 Thijs

- Write extended radiation (when it's done)
- Rewrite availability part
- Implement flow chart in the introduction.
- Implement suggestions
- Send around for final check
- Send to GMDD

1.2 Chiel

- Write revised surface paragraph (when it's done)

1.3 Stephan

- Release DALES3.2 (when chemistry, radiation and LSM are there).

Correspondence to: Thijs Heus
(heus@knmi.nl)

2 Introduction

Modern atmospheric research typically relies on a cascade of observational and modeling tools. The largest-scale models, such as the General Circulation Models (GCM), contain parameterizations that were developed with the help of observational campaigns, but more and more also with the help of limited area modeling. With respect to the atmospheric boundary layer (ABL), Large-Eddy Simulations (LES) are arguably the most detailed type of numerical modeling available.

The principle of LES is to resolve the turbulent scales larger than a certain filter width, and to parameterize the smaller, less energetic scales. This filter width is usually related to the grid size of the LES, and ranges typically between $1\mathrm{m}$ for stably stratified boundary layers, to $50\mathrm{m}$ for simulations of the cloud-topped ABL. In such a typical LES set up, up to 90% of the turbulent energy resides in the resolved scales. In the fields where LES is applicable, it has the advantage over coarser models that LES relies only weakly on parameterizations. In comparison with observational studies, LES has the advantage of providing a complete data set, in terms of time, space, and in terms of diagnosable variables. Especially the combined use of LES and observations is a popular methodology in process studies of the ABL.

LES modeling of the ABL started in the late sixties (e.g., Lilly, 1967; Deardorff, 1972); cloudy boundary layers were first simulated by Sommeria (1976). From Nieuwstadt and Brost (1986) onward, several cycles of intercomparison studies compare state-of-the-art LES models with observational studies and with each other. The aim of these studies was not so much to determine which LES model performs best in which situation, but more to determine where the general strong points of atmospheric LES lies, and in what fields LES still has room for improvement. Two particularly active cycles are organised under the umbrella of the Global Energy and Water Cycle Experiment (GEWEX): the GEWEX Atmo-

spheric Boundary Layers Study (GABLS), and the GEWEX Cloud System Study (GCSS) Boundary Layer Cloud Working Group. The GABLS focusses on the clear boundary layer, mainly on stable and transitional situations (Holtslag, 2006; Beare et al., 2006; Basu et al., 2008). The GCSS looks at different aspects of boundary layer clouds, mainly shallow cumulus and stratocumulus clouds (Bretherton et al., 1999b,a; Duynkerke et al., 1999, 2004; Brown et al., 2002; Siebesma et al., 2003; Stevens et al., 2001, 2005; Ackerman et al., 2009; van Zanten et al., 2009).

The Dutch Atmospheric Large-Eddy Simulation (DALES) has joined in virtually all of these intercomparisons. Besides convective, stable and cloud-topped boundary layers, DALES has also been used on a wide range of topics, such as studies of shear driven flow, heterogeneous surfaces, dispersion and turbulent reacting flows in the ABL, and of flow over sloped terrain. As such, DALES is one of the most allround tested available LES models for studies of the ABL. In this paper, we aim to describe and validate DALES3.2, the current version of DALES.

In the remainder of this paper, we first give a thorough description of the code in section 3. In section 4, an overview of studies condcuted with DALES are given, both as a validation of the code as well as an overview of the capabilities of an LES like DALES. In section 5, an outlook is given on future studies that are planned to be done DALES, as well as an outlook on future improvements.

3 Description of the code

3.1 Generalities

DALES is rooted in the LES of Nieuwstadt and Brost (1986). Cuijpers and Duynkerke (1993) first used DALES for moist convection, and provide a general description of an older version of DALES. Large parts of the code have been changed ever since and contributions of many people over a number of years have resulted in the current version 3.2 of DALES. Currently, DALES is maintained by researchers from (alphabetically) Delft University, the Royal Netherlands Meteorological Institute (KNMI), and Wageningen University.

Notable changes in comparison with the version that has been described by Cuijpers and Duynkerke (1993), include: Different time integration and advection schemes, revised subfilter-scale, surface, and radiation schemes, addtion of a cloud-microphysical scheme, capabilities for chemical reactive scalar transport and for Lagrangian particle dispersion, for flow over heterogeneous and for flow over sloped terrain. These revisions in DALES result in faster simulations and higher stability, and in an easier and more extendable user interface. Due to the modular setup of the code, newly written code for specific applications of DALES can easily improve the code as a whole. This makes DALES suitable as a community model; besides the actively developing core users, the model is currently used in several other institutes across the world.

DALES3.2 is released under the GPLv3 license. It is available at www.ablresearch.org/dales after registration. Documentation is also available there. Registration is necessary to keep track of the user base for dissemination of bug reports and fixes. Although the code is completely free to use, to modify and to redistribute, it is regarded courtesy to share bug fixes and extensions that can be of general interest, and to keep in contact with the core developers, also in case of publications.

DALES is written in Fortran 95. The only dependency of DALES are on makedepf90 for building (packeged with the code), and on the Message Passing Protocol (MPI). Some optional modules also require NetCDFv3. Code for Fourier transformations is provided as well, leaving DALES as portable as possible. To the best knowledge of the authors, DALES runs on all common combinations of platform architecture, compiler, and MPI implementation. Currently, an effort is being made to port DALES to nVidia graphical processors, using CUDA (Griffith et al., 2009).

The prognostic variables of DALES are the three velocity components u_i, the liquid water potential temperature θ_l, the total water specific humidity q_t, the rain water specific humidity q_r, the rain droplet number concentration N_r, and up to 100 passive or reactive scalars. Because of the one-and-a-half order scheme that parameterizes sub-filter scale dynamics, the subfilter-scale turbulent kinetic energy (SFS-TKE, e) counts as an additional prognostic variable. To decrease simulation time, most prognostic variables can be switched of; only calculations of u_i, e, and θ_l are obligatory.

Given that ice is not currently implemented in the model, the total water specific humidity is defined as the sum of the water vapor specific humidity q_v and the cloud liquid water specific humidity q_c:

$$q_t = q_v + q_c \tag{1}$$

Note that this definition excludes the rain water specific humidity q_r from q_t. Any conversion between rain water on the one hand, and cloud water or water vapor on the other hand, will therefore enter the equations for q_t and for θ_l as an addition source term. As a definition of θ_l, we use the close approximation explained by Emanuel (1994):

$$\theta_l \approx \theta - \frac{L}{c_{pd}\Pi} q_c \tag{2}$$

with $L = 2.5 \times 10^6 \mathrm{J\ kg^{-1}}$ the latent heat release of vaporization, $c_{pd} = 1004 \mathrm{J\ kg^{-1}\ K^{-1}}$ the heat capacity of dry air, and Π the exner function:

$$\Pi = \left(\frac{p}{p_0}\right)^{\frac{R_d}{c_{pd}}}. \tag{3}$$

In which $R_d = 287.0 \mathrm{J\ kg^{-1}\ K^{-1}}$ is the gas constant for dry air.

R_v	Gas constant for water vapor	$461.5\text{J kg}^{-1}\text{ K}^{-1}$
R_d	Gas constant for dry air	$287.0\text{J kg}^{-1}\text{ K}^{-1}$
L	Latent heat release for vaporization	$2.5\times10^6\text{J kg}^{-1}$
c_{pd}	Heat capacity for dry air	$1004\text{J kg}^{-1}\text{ K}^{-1}$

Table 1. The main thermodynamical constants used throughout this paper.

In the absence of precipitation and other explicit source terms, θ_l and q_t are conserved variables. The virtual potential temperature θ_v is in good approximation defined with:

$$\theta_v \approx \left(\theta_l + \frac{L}{c_{pd}\Pi}q_c\right)\left(1-\left(1-\frac{R_v}{R_d}\right)q_t - \frac{R_v}{R_d}q_c\right), \quad (4)$$

with $R_v = 461.5\text{J kg}^{-1}\text{ K}^{-1}$, the gas constants for water vapor. The most important thermodynamical constants that are used throughout this paper are summarized in Tab. 1

DALES assumes the Boussinesq approximation, and is run on an Arakawa C-grid (see Fig. 2). The pressure, the SFS-TKE, and the scalars are defined at cell center, the 3 velocity components are defined at the West side, the South side, and the bottom side of the grid cell, respectively.

In the remainder of this article, quantities that are averaged over the LES-filter are denoted with a tilde $\widetilde{\cdot}$, time averages with a overbar $\overline{\cdot}$, and averages over the two horizontal directions of the domain with angular brackets $\langle\cdot\rangle$ (slab average). The prognostic scalars can often be treated simultaneously as the generic scalar field $\varphi \in \{\theta_l, q_t, q_r, N_r, s_n\}$. Primes denote the subfilter-scale fluctuations with respect to the filtered mean. To remain consistent with notational conventions as used in literature and also in the source code of DALES, some symbols can have different meaning between different subsections. In such cases, the immediate context should always make it clear what each symbol stand for in a particular section. Vertical velocities and fluxes are in general directed upward; only the radiative and sedimentation fluxes point downward, following conventions.

3.2 The governing equations

Within the Boussinesq approximation the equations of motion, after application of the LES filter, are given by

$$\frac{\partial\widetilde{u}_i}{\partial x_i} = 0, \quad (5)$$

$$\frac{\partial\widetilde{u}_i}{\partial t} = -\frac{\partial\widetilde{u}_i\widetilde{u}_j}{\partial x_j} - \frac{\partial\pi}{\partial x_i} + \frac{g}{\theta_0}(\widetilde{\theta_v}-\theta_0)\delta_{i3} + \mathcal{F}_i - \frac{\partial\tau_{ij}}{\partial x_j}, \quad (6)$$

$$\frac{\partial\widetilde{\varphi}}{\partial t} = -\frac{\partial\widetilde{u}_j\widetilde{\varphi}}{\partial x_j} - \frac{\partial R_{u_j,\varphi}}{\partial x_j} + \mathcal{S}_\varphi, \quad (7)$$

where the tildes denotes the filtered mean variables. Viscous transport terms have been neglected. The z-direction (x_3) is taken to be vertical. θ_0 is the reference state potential temperature and $\mathcal{F}_i$ represents other forcings, including large scale forcings and the Coriolis forcing

$$\mathcal{F}_i^{\text{cor}} = -2\epsilon_{ijk}\Omega_j\widetilde{u_k}, \quad (8)$$

where $\mathbf{\Omega}$ is the earth's angular velocity. Source terms for scalar φ are denoted by $\mathcal{S}_\varphi$, and may include of microphysical ($\mathcal{S}^{\text{mcr}}$), radiative ($\mathcal{S}^{\text{rad}}$), chemical ($\mathcal{S}^{\text{chem}}$), large-scale ($\mathcal{S}^{\text{ls}}$), and relaxation ($\mathcal{S}^{\text{rel}}$) terms. The subfilter-scale (SFS), or residual, scalar fluxes are denoted by $R_{u_j,\varphi} \equiv \widetilde{u_j\varphi} - \widetilde{u}_j\widetilde{\varphi}$, i.e., the contribution to the resolved motion from all scales below the LES filter width. The anisotropic SFS-stress tensor is defined by

$$\tau_{ij} \equiv \widetilde{u_iu_j} - \widetilde{u}_i\widetilde{u}_j - \frac{2}{3}\delta_{ij}e, \quad (9)$$

where $e = \frac{1}{2}(\widetilde{u_iu_i} - \widetilde{u}_i\widetilde{u}_i)$ is the subfilter-scale turbulent kinetic energy (SFS-TKE). Formally, the trace of the SFS-stress has been included in the modified pressure

$$\pi = \frac{1}{\rho}(\widetilde{p}-p_0) + \frac{2}{3}e. \quad (10)$$

To enforce continuity (Eq. 5), a Poisson equation for π is solved

$$\frac{\partial^2\pi}{\partial x_i^2} = \frac{\partial}{\partial x_i}\left(-\frac{\partial\widetilde{u}_i\widetilde{u}_j}{\partial x_j} + \frac{g}{\theta_0}(\theta_v-\theta_0)\delta_{i3} - 2\epsilon_{ijk}\Omega_j\widetilde{u_k} + \mathcal{F}_i - \frac{\partial\tau_{ij}}{\partial x_j}\right). \quad (11)$$

Since computations are performed in a double periodic domain, the Poisson equation is solved by applying a Fast Fourier Transform in the homogenous directions followed by solving a tridiagonal system in the z-direction. A schematic overview of how the different processes affect the different variables is given in Fig. 1.

3.3 Subfilter-scale Model

The SFS stress tensor and scalar fluxes are modeled using one-and-a-half order closure (Deardorff, 1973):

$$\tau_{ij} = -K_m\left(\frac{\partial\widetilde{u}_i}{\partial x_j} + \frac{\partial\widetilde{u}_j}{\partial x_i}\right), \quad (12)$$

$$R_{u_j,\varphi} = -K_h\frac{\partial\widetilde{\varphi}}{\partial x_j}, \quad (13)$$

with the eddy diffusivity coefficients K_m and K_h being a function of e. The prognostic equation for e:

$$\frac{\partial e}{\partial t} = -\widetilde{u}_j\frac{\partial e}{\partial x_j} - \tau_{ij}\frac{\partial\widetilde{u}_i}{\partial x_j} + \frac{g}{\theta_0}R_{w,\theta_v} - \frac{\partial R_{u_j,e}}{\partial x_j} - \frac{1}{\rho_0}\frac{\partial R_{u_j,p}}{\partial x_j} - \varepsilon, \quad (14)$$

with ε the dissipation rate. To close Eq. 14, we need to parameterize all the right-hand-side terms but the first one. The

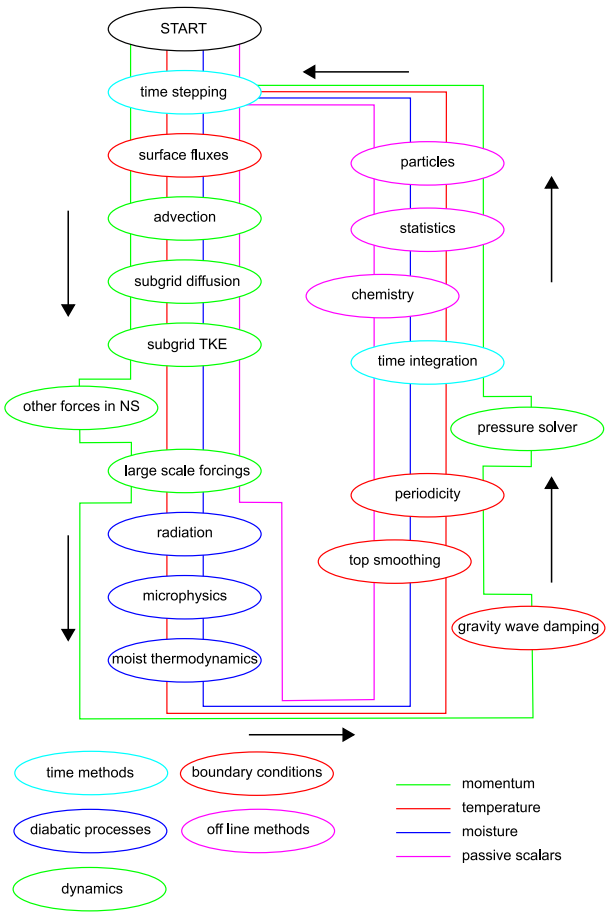

Fig. 1. Flowchart of DALES.

SFS-TKE production by shear (the second term) is closed with Eq. 12. Following Deardorff (1980), we use for the third term, the production due to buoyancy:

$$\frac{g}{\theta_0} R_{w,\theta_v} = \frac{g}{\theta_0} \left(A R_{w,\theta_l} + B R_{w,q_t} \right), \tag{15}$$

with coefficients A and B depending on the local thermodynamic state (dry or wet):

$$\left.\begin{aligned} A &= A_d = \tfrac{R_v}{R_d}\widetilde{q_t} \\ B &= B_d = \left(\tfrac{R_v}{R_d} - 1\right)\theta_0 \end{aligned}\right\} \text{ if } q_c = 0 \tag{16}$$

$$\left.\begin{aligned} A &= A_w = \frac{(1-\widetilde{q_t}+q_s\frac{R_v}{R_d}\left(1+\frac{L}{R_v T}\right)}{\frac{1+L^2 q_s}{c_{pd} R_v T^2}} \\ B &= B_w = A_w \tfrac{L}{c_{pd}} - T \end{aligned}\right\} \text{ if } q_c > 0. \tag{17}$$

where q_s is the saturation specific humidity at the given temperature. At a cloud interface, it is a matter of choice whether to use the dry or the wet coefficients in calculation of the buoyancy production. Especially in situations where the properties of the cloud deck are around the cloud-top entrainment instability (CTEI) criterion, this choice proves to be critical (Randall, 1980; Bretherton et al., 2004; de Roode, 2007). To solve this, we determine the critical mixing ratio χ_*:

$$\chi_* = \frac{\left(A_d \frac{L}{c_{pd}} - \frac{R_v}{R_d}\widetilde{\theta_l}\right) q_c}{\left(A_w - A_d\right) \Delta\widetilde{\theta_l} \left(B_w - B_d\right) \Delta\widetilde{q_t}}, \tag{18}$$

where $\Delta\widetilde{\theta_l} = \widetilde{\theta_l}(z+\Delta z) - \widetilde{\theta_l}(z-\Delta z)$ and $\Delta\widetilde{q_t} = \widetilde{q_t}(z+\Delta z) - \widetilde{q_t}(z-\Delta z)$ are the differences over the cloud interface. If χ_* is smaller than 0.5, the dry coefficients are used to determine the SFS buoyancy production. If $\chi_* > 0.5$, the wet coefficients are used.

The fourth and fifth term in Eq. 14 are together parameterized as

$$-\frac{\partial}{\partial x_j}\left(R_{u_j,e} + \frac{1}{\rho_0} R_{u_j,p}\right) = \frac{\partial}{\partial x_j}\left(2K_m \frac{\partial e}{\partial x_j}\right), \tag{19}$$

Under the assumption of 3D homogenous isotropic turbulence, and for a sharp spectral cutoff filter, a relation between the dissipation rate ε and the SGS-TKE e can be found by integration of the energy spectrum $E(k) = \alpha\varepsilon^{2/3}k^{-5/3}$ from a filter wavenumber k_f, that lies within the inertial subrange, to infinity. This leads to

$$\varepsilon = e^{3/2} k_f \left(\frac{3}{2}\alpha\right)^{-3/2}, \tag{20}$$

with $\alpha = 1.5$ denoting the Kolmogorov constant. The production of SFS-TKE due to shear is equal to:

$$\begin{aligned} \mathcal{P} &= 2K_m \int_0^{k_f} k^2 E(k) dk \\ &= \frac{3}{2} K_m \alpha \varepsilon^{2/3} k_f^{4/3}. \end{aligned} \tag{21}$$

The eddy diffusivity for momentum can be found by equating locally the shear-production of SFS-TKE to the dissipation:

$$\mathcal{P} = \varepsilon$$

This yields for K_m

$$\begin{aligned} K_m &= \frac{e^{1/2}}{k_f}\left(\frac{3}{2}\alpha\right)^{-3/2} = c_m \lambda e^{1/2}, \\ &\text{with } c_m = \frac{c_f}{2\pi}\left(\frac{3}{2}\alpha\right)^{-3/2} \end{aligned} \tag{22}$$

where we defined the filter width $c_f\lambda = \frac{2\pi}{k_f}$. The eddy diffusivity for heat is modeled similarly as $K_h = c_h \lambda e^{1/2}$, and for the dissipation ε we can write:

$$\varepsilon = \frac{c_\varepsilon}{\lambda} e^{3/2}, \text{ with } c_\varepsilon = \frac{2\pi}{c_f}\left(\frac{3}{2}\alpha\right)^{-3/2} \tag{23}$$

In unstable flow, $c_f\lambda$ can be taken proportional to the grid size:

$$\lambda = \Delta = (\Delta x \Delta y \Delta z)^{1/3}, \tag{24}$$

$$c_f = 2.5, \tag{25}$$

α	c_f	$c_{\varepsilon,1}$	$c_{\varepsilon,2}$	c_m	$c_{h,1}$	$c_{h,2}$	c_N
1.5	2.5	0.19	0.51	0.12	1	2	0.76

Table 2. An overview of the parameters used in the SFS scheme of DALES model. Not all parameters are independent.

see Cuijpers (1990). However, this no longer holds for stable situations, i.e., when $\frac{\partial \theta_v}{\partial z} > 0$. In that case, λ is taken to be

$$\lambda = \min\left(\Delta, c_N \frac{e^{1/2}}{N}\right), \tag{26}$$

with $N^2 = \frac{g}{\theta_0}\frac{\partial \theta_v}{\partial z}$ denoting the Brunt-Väisälä frequency, and $c_N = 0.76$. A stability correction is also applied on c_h and c_ε:

$$c_h = \left(c_{h,1} + c_{h,2}\frac{\lambda}{\Delta}\right) c_m, \tag{27}$$

$$c_\varepsilon = c_{\varepsilon,1} + c_{\varepsilon,2}\frac{\lambda}{\Delta}. \tag{28}$$

Now all parameters of the subfilter-scale parameterization of DALES are defined; they are summarized in Tab. 2.

Substituting the closure relations and parameters into Eq. 14, one can a derive a prognostic equation for $e^{1/2}$:

$$\begin{aligned}\frac{\partial e^{1/2}}{\partial t} = &-\widetilde{u_j}\frac{\partial e^{1/2}}{\partial x_j} + \frac{1}{2e^{1/2}}\left[K_m\left(\frac{\partial \widetilde{u}_j}{\partial x_i} + \frac{\partial \widetilde{u}_i}{\partial x_j}\right)\frac{\partial \widetilde{u}_i}{\partial x_j}\right.\\ &\left. - K_h\frac{g}{\theta_0}\frac{\partial (A\widetilde{\theta_l} + B\widetilde{q_t})}{\partial z}\right]\\ &+\frac{\partial}{\partial x_j}\left(2K_m\frac{\partial e^{1/2}}{\partial x_j}\right) - \frac{c_\varepsilon e}{2\lambda},\end{aligned} \tag{29}$$

which closes the system.

3.4 Surface Model

The LES model contains a set of options to solve the interaction of the turbulent flow with its bottom boundary. As DALES has a no-slip boundary at the bottom, but does not resolve the flow to the scale of the molecular friction, it requires a model to parameterize the turbulent drag and the exchange of scalars between the surface and the atmosphere. The surface fluxes enter the domain at subfilter-scale, since by definition the resolved fluctuations in the vertical velocity at the surface are equal to zero.

We followed the common way of parameterizing turbulent fluxes in atmospheric models by applying the transfer laws as given by Louis (1979)

$$u_*^2 = \sqrt{\widetilde{u'w'}^2 + \widetilde{v'w'}^2} = C_m U^2 \tag{30}$$

$$\widetilde{w'\varphi'} = -C_\varphi U\left(\varphi_s - \widetilde{\varphi}\right) \tag{31}$$

where u_* is the friction velocity, u and v are the two horizontal components of the total horizontal wind $U = \sqrt{\widetilde{u}^2 + \widetilde{v}^2}$, φ_s is the surface value of scalar φ, and C_m and C_φ the drag coefficients for momentum and scalars, respectively.

In DALES we assume that the first model level is in the atmospheric surface layer. Therefore, we can apply the scaling arguments of Businger et al. (1971); Yaglom (1977); Stull (1988), who used Monin-Obukhov similarity theory to show that in this layer the following relations hold:

$$u_* = \frac{\kappa U}{\ln\left(\frac{z_1}{z_{0m}}\right) - \Psi_m\left(\frac{z_1}{L}\right) + \Psi_m\left(\frac{z_{0m}}{L}\right)} \tag{32}$$

$$\varphi_* = -\frac{\widetilde{w'\varphi'}}{u_*} = \frac{\kappa\left(\widetilde{\varphi} - \varphi_s\right)}{\ln\left(\frac{z_1}{z_{0\varphi}}\right) - \Psi_\varphi\left(\frac{z_1}{L}\right) + \Psi_\varphi\left(\frac{z_{0h}}{L}\right)} \tag{33}$$

in which z_{0m} and $z_{0\varphi}$ are the roughness lengths for momentum and an arbitrary scalar, z_1 is the height of the first model level and $U(z_1)$ and $\widetilde{\varphi}(z_1)$ the horizontal wind and the value of the scalar at this height. Ψ_m and Ψ_φ are the integrated flux gradient relationships and

$$L = -\frac{u_*^3}{\kappa\frac{g}{\theta_0}\widetilde{w'\theta'_{v0}}} \tag{34}$$

is the Obukhov length, with $\kappa = 0.4$ the von Karman constant. DALES uses the functions for Ψ_m and Ψ_φ as provided by Beljaars (1991).

In DALES u_*, L and, optionally, the characteristic scalar scales φ_* and moisture scale q_* are determined iteratively, as there is a circular dependence between these variables. Per time step a slab averaged value for these variables is derived based on horizontally averaged wind and scalar gradients. Now, we can calculate mean drag coefficents C_m and C_φ by:

$$C_m = \frac{u_*^2}{\langle U^2\rangle} \tag{35}$$

$$C_\varphi = \frac{u_*\varphi_*}{\langle U\rangle\left(\langle\widetilde{\varphi}\rangle - \varphi_s\right)} \tag{36}$$

Although all locations in the horizontal use the same drag coefficient, we calculate local fluxes by using the local values of the wind and scalars. The subfilter-scale momentum fluxes are calculated by decomposing Eq. 30 along the two components of the horizontal wind vector, whereas Eq. 31 gives the scalar flux. This results in

$$\widetilde{u'w'} = -C_m U\widetilde{u} \tag{37}$$

$$\widetilde{v'w'} = -C_m U\widetilde{v} \tag{38}$$

$$\widetilde{w'\varphi'} = -C_\varphi U\left(\widetilde{\varphi} - \varphi_s\right) \tag{39}$$

DALES has three options to parameterize the fluxes at the bottom boundary:

1. *Parameterized surface scalar and momentum fluxes, prescribed surface values*. In this option u_*, L and φ_* are solved iteratively to get the drag coefficients.

This option is often associated with studies of the marine boundary layer, in which the surface temperature is nearly constant during the time scale of an LES simulation. In combination with a transient temperature, it is also applied in the simulation of stable boundary layers.

2. *Prescribed surface scalar fluxes, prescribed* u_*. In this option no iterations are necessary and the scalar surface values φ_s are calculated diagnostically. This is an option that is commonly used in simulations of free convection where $u_* = 0$.

3. *Prescribed surface scalar fluxes, parameterized* u_*. Here u_* and L are resolved by iteration, whereas φ_* is diagnostically as a function of the prescribed scalar fluxes and the calculated u_*. This is the preferred option for daytime convection over land in situations containing a large scale pressure gradient.

Prescribed fluxes or surface values may depend on time; linear interpolation is then performed between the given 'anchor' points.

In addition to the previous description which treated homogeneous surfaces, DALES is also able to simulate heterogeneously forced ABLs. Under such conditions, only the prescribed scalar fluxes boundary conditions are available. Each grid cell has then its own value for the scalar flux, whereas the momentum flux is dynamically computed.

3.5 Other boundary conditions

Besides the surface-layer modeling, the boundary conditions at the top of the domain and in the horizontal directions are relatively straightforward. In the horizontal directions, periodic boundary conditions are applied. At the top of the domain, we take:

$$\frac{\partial \widetilde{u}}{\partial z} = \frac{\partial \widetilde{v}}{\partial z} = 0; \qquad \widetilde{w} = 0; \qquad \frac{\partial \widetilde{\varphi}}{\partial z} = \mathrm{cst}. \tag{40}$$

Horizontal fluctuations at the top of the domain (for instance gravity waves) are damped out by a sponge layer through an additional forcing/source term:

$$\mathcal{F}_i^{\mathrm{sp}}(z) = -\frac{1}{t^{\mathrm{sp}}}\left(\langle \widetilde{u}_i \rangle - \widetilde{u}_i\right), \tag{41}$$

$$\mathcal{S}_\varphi^{\mathrm{sp}}(z) = -\frac{1}{t^{\mathrm{sp}}}\left(\langle \varphi \rangle - \varphi\right), \tag{42}$$

with t^{sp} a relaxation time scale that goes from $t_0^{\mathrm{sp}} = 1/(2.75 \times 10^{-3})\mathrm{s} \approx 6\mathrm{min}$ at the top of the domain to infinity at the bottom of the sponge layer.

3.6 Numerical scheme

A Cartesian grid is used, with optional grid stretching in the $\hat{z}$ direction. For clarity, an equidistant grid is assumed in the discussion of the advection scheme. The grid is staggered in space, on an Arakawa C-grid; the pressure, the SFS-TKE and the scalars are defined at $\boldsymbol{x}+\frac{1}{2}(\Delta x, \Delta y, \Delta z)$, the $\widetilde{u}$ is defined at $\boldsymbol{x} + \frac{1}{2}(0, \Delta y, \Delta z)$, and similar for $\widetilde{v}$ and $\widetilde{w}$. The level of cell center is called the full level (denoted with an 'f'); the level where w is located is called the half level (an 'h'). The (variable) vertical grid spacing Δz is defined centered around the belonging level (see Fig. 2).

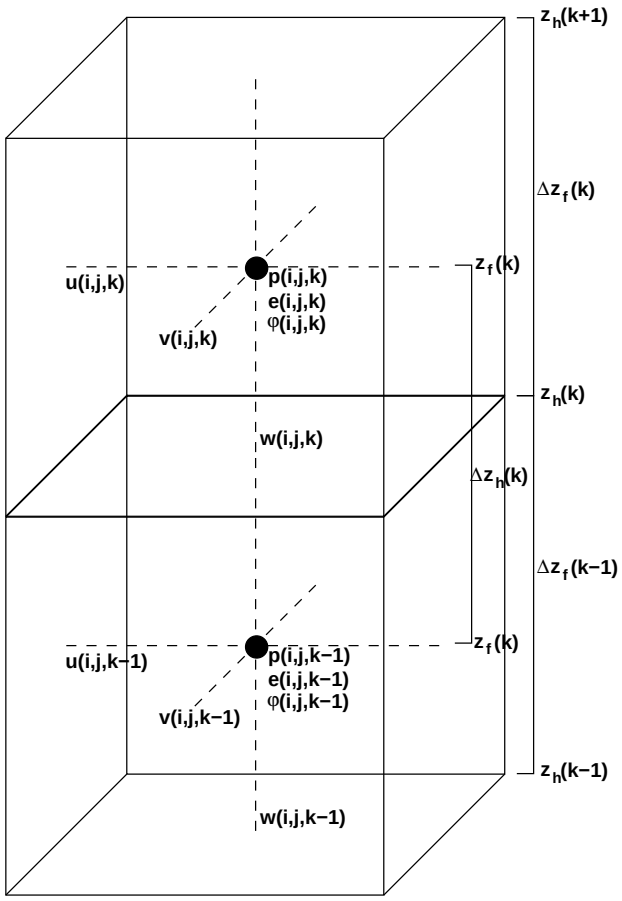

Fig. 2. The Arakawa C-grid as used in DALES. Pressure, SFS-TKE and the scalars are defined at cell-center, the 3 velocity components at the face of the cell. The level of cell center is called the full level (denoted with an 'f'); the level where w is located is called the half level (an 'h'). The (variable) vertical grid spacing Δz is defined centered around the belonging level.

Time integration is done by a third order Runge-Kutta scheme following Wicker and Skamarock (2002). With $f^n(\phi^n)$ the right-hand side of the appropriate equation of Eqs. 6-7 for variable $\phi = \{\widetilde{u}, \widetilde{v}, \widetilde{w}, e^{1/2}, \widetilde{\varphi}\}$, ϕ^{n+1} at $t + \Delta t$ is calculated in three steps:

$$\begin{aligned} \phi^* &= \phi^n + \frac{\Delta t}{3} f^n(\phi^n) \\ \phi^{**} &= \phi^n + \frac{\Delta t}{2} f^*(\phi^*) \\ \phi^{n+1} &= \phi^n + \Delta t f^{**}(\phi^{**}), \end{aligned} \tag{43}$$

with the asterisks denoting intermediate time steps. The size

of the timestep Δt is determined adaptively, and is limited by both the Courant-Friedrichs-Lewy criterion (CFL)

$$\mathrm{CFL} = \max\left(\left|\frac{u_i \Delta t}{\Delta x_i}\right|\right), \tag{44}$$

and the diffusion number d (see Wesseling (1996)).

$$d = \max\left(\sum_i \frac{K_m \Delta t}{\Delta x_i^2}\right). \tag{45}$$

The numerical stability and accuracy depends on the spatial scheme that is used. Therefore, the limiting CFL and d numbers can be adjusted to further optimize the timestep.

Depending on the desired properties (like high accuracy or monotonicity), several advection schemes are available. With advection in the $\hat{x}$ direction discretized as

$$\frac{\partial \widetilde{u}_i \phi_i}{\partial x} = \frac{F_{i+\frac{1}{2}} - F_{i-\frac{1}{2}}}{\Delta x}, \tag{46}$$

with $F_{i-\frac{1}{2}}$ the convective flux of variable ϕ through the $i-\frac{1}{2}$ plane. Since we are using a staggered grid, the velocity is available at $i-\frac{1}{2}$ without interpolation. Second order central differencing can be used for variables where neither very high accuracy nor strict monotonicity is necessary:

$$F^{2nd}_{i-\frac{1}{2}} = \widetilde{u}_{i-\frac{1}{2}} \frac{\phi_i + \phi_{i-1}}{2}, \tag{47}$$

A higher-order accuracy in the calculation of the advection is reached with a sixth order central differencing scheme (see Wicker and Skamarock, 2002):

$$F^{6th}_{i-\frac{1}{2}} = \frac{\widetilde{u}_{i-\frac{1}{2}}}{60}\left[37(\phi_i + \phi_{i-1}) - 8(\phi_{i+1} + \phi_{i-2}) + (\phi_{i+2} + \phi_{i-3})\right]. \tag{48}$$

By adding a small dissipative term to $F^{6th}_{i-\frac{1}{2}}$, a fifth order scheme is created that is nearly monotone:

$$F^{5th}_{i-\frac{1}{2}} = F^{6th}_{i-\frac{1}{2}} - \left|\frac{\widetilde{u}_{i-\frac{1}{2}}}{60}\right|\left[10(\phi_i - \phi_{i-1}) - 5(\phi_{i+1} - \phi_{i-2}) + (\phi_{i+2} - \phi_{i-3})\right]. \tag{49}$$

For advection of scalars that need to be strictly monotone (for example chemically reacting species) the κ scheme Hundsdorfer et al. (1995) has been implemented:

$$F^{\kappa}_{i-\frac{1}{2}} = \widetilde{u}_{i-\frac{1}{2}}\left[\phi_{i-1} + \frac{1}{2}\kappa_{i-\frac{1}{2}}\left(\phi_{i-1} - \phi_{i-2}\right)\right], \tag{50}$$

in case $\widetilde{u} > 0$. Following Hundsdorfer et al. (1995), $\kappa_{i-1/2}$ serves as a switch between higher order advection and first order upwind in case of strong upwind gradients of ϕ. This makes the scheme monotone, but also rather dissipative.

3.7 Cloud microphysics

The cloud-microphysical scheme implemented in DALES is a bulk scheme for precipitating liquid-phase clouds. The droplet spectrum is divided in a cloud and a rain category.

The cloud liquid water specific humidity q_c is diagnosed using a classic saturation adjustment. The cloud droplet number concentration N_c is a fixed parameter that can be adjusted according to the degree of pollution of the cloud, meaning that the activation process is not taken in account.

The precipitation scheme is based on Seifert and Beheng (2001, hereafter SB01) two-moment bulk scheme developed for heavy precipitating warm clouds. Rain drop spectra are characterized by the rain drop number concentration $\widetilde{N_r}$ and the rain drop water specific humidity $\widetilde{q_r}$. SB01 assumes the limit between the cloud category and the rain category at the separating mass value x_0 of $2.6 \times 10^{-10}\mathrm{kg}$ which corresponds to a separating radius r_0 of the order of $40\mu\mathrm{m}$. In slightly precipitating stratocumulus, most of the falling mass is contained in particles smaller than $50\mu\mathrm{m}$ in radius, also referred to as drizzle. Thus the SB01 scheme is more suitable for heavily precipitating clouds, in which most of the falling mass is contained in millimeter size particles. The Khairoutdinov and Kogan (2000) scheme, in which the limit is set at the smaller radius value of $25\mu\mathrm{m}$ and developed specially for stratocumulus clouds has been implemented too in DALES. This low value of r_0 permits consideration of drizzle in the precipitating category, which can have significant impact on the evolution of the cloud. Parameterizations are expressed as a function of local microphysical values. Thus the schemes are valid only for simulations where microphysical fields are explicitly resolved, as is the case in LES. Resolution must not be more than $200\mathrm{m}$ horizontally and a few ten of meters vertically.

The conversion rates that impact rain formation and evolution are parameterized according to SB01, Seifert and Beheng (2006, hereafter SB06), and Seifert (2008). For each prognostic variable modified in microphysics, the source term due to microphysical processes $\mathcal{S}^{\mathrm{mcr}}$ consists of autoconversion (au), accretion (ac), rain drop selfcollection (sc), break-up (bu), rain sedimentation (ser), cloud droplet sedimentation (ser), and rain evaporation (evr):

$$\begin{array}{llll} \mathcal{S}^{\mathrm{mcr}}_{q_t} = \mathcal{S}^{\mathrm{au}}_{q_t} + & \mathcal{S}^{\mathrm{acc}}_{q_t} + & & \mathcal{S}^{\mathrm{sec}}_{q_t} + \mathcal{S}^{\mathrm{evr}}_{q_t} \\ \mathcal{S}^{\mathrm{mcr}}_{\theta_l} = \mathcal{S}^{\mathrm{au}}_{\theta_l} + & \mathcal{S}^{\mathrm{acc}}_{\theta_l} + & & \mathcal{S}^{\mathrm{sec}}_{\theta_l} + \mathcal{S}^{\mathrm{evr}}_{\theta_l} \\ \mathcal{S}^{\mathrm{mcr}}_{N_r} = \mathcal{S}^{\mathrm{au}}_{N_r} + & & \mathcal{S}^{\mathrm{sc}}_{N_r} + \mathcal{S}^{\mathrm{br}}_{N_r} + & \mathcal{S}^{\mathrm{ser}}_{N_r} + \mathcal{S}^{\mathrm{evr}}_{N_r} \\ \mathcal{S}^{\mathrm{mcr}}_{q_r} = \mathcal{S}^{\mathrm{au}}_{q_r} + & \mathcal{S}^{\mathrm{acc}}_{q_r} + & & \mathcal{S}^{\mathrm{ser}}_{q_r} + \mathcal{S}^{\mathrm{evr}}_{q_r}. \end{array} \tag{51}$$

Microphysical tendencies in $\widetilde{\theta_l}$ can be expressed directly in function of $\widetilde{q_t}$ tendencies:

$$\mathcal{S}^{\mathrm{mcr}}_{\theta_l} = -\frac{L}{c_{p,d}\Pi}\mathcal{S}^{\mathrm{mcr}}_{q_t}. \tag{52}$$

The prognostic thermodynamical variables, microphysical variables, processes and parameterizations are summarized

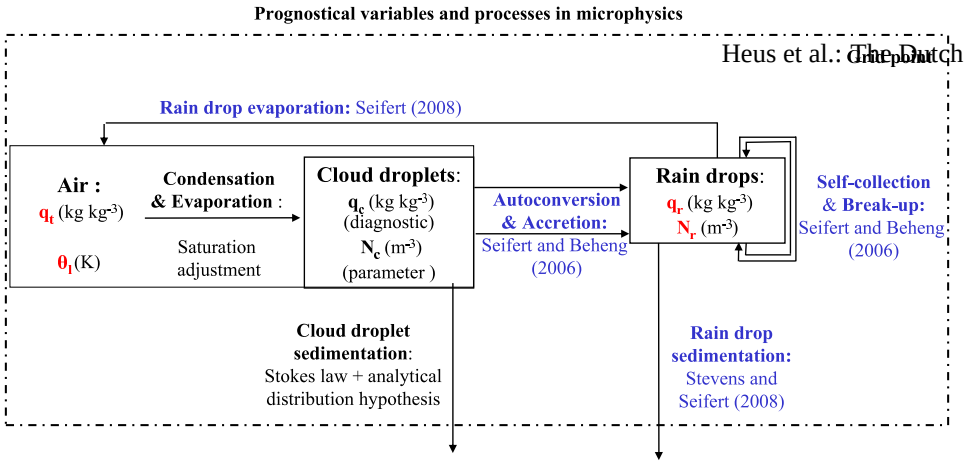

Fig. 3. Representation of the prognostic thermodynamical variables $\widetilde{\theta}_l$, $\widetilde{q}_t$, the microphysical parameter and variables N_c, q_c, $\widetilde{N}_r$, $\widetilde{q}_r$, and the microphysical processes relating these variables.

in Fig. 3. The conversion rates that impact rain formation and evolution are parameterized according to SB01, Seifert and Beheng (2006, hereafter SB06), and Seifert (2008). The cloud water specific humidity is diagnosed from the cloud condensation and evaporation scheme.

3.7.1 Cloud water condensation and evaporation

The cloud specific humidity q_c is diagnosed from pressure, temperature and total specific humidity using an "all or nothing cloud adjustment scheme: it is assumed that there is no cloud water present in an unsaturated grid box, while all moisture above saturation value $\widetilde{q}_s$ is cloud water:

$$q_c = \begin{cases} \widetilde{q}_t - \widetilde{q}_s \text{ if } \widetilde{q}_t > \widetilde{q}_s \\ 0 \qquad \text{otherwise.} \end{cases} \tag{53}$$

To calculate $\widetilde{q}_s \equiv \widetilde{q}_s(\widetilde{T}, p)$, an implicit equation needs to be solved, because $\widetilde{T}$ is not directly available and has to be diagnosed from the prognostic variables θ_l and q_t. $\widetilde{T}$ is approximated with help of the liquid water temperature $\widetilde{T}_l$, which is equal to:

$$\widetilde{T}_l = \Pi \widetilde{\theta}_l. \tag{54}$$

Following Sommeria and Deardorff (1977), $\widetilde{q}_s(\widetilde{T}, p)$ is found through a Taylor expansion around $\widetilde{q}_{sl} \equiv \widetilde{q}_s(\widetilde{T}_l, p)$:

$$\widetilde{q}_s(\widetilde{T}, p) = \widetilde{q}_s(\widetilde{T}_l, p) + (\widetilde{T} - \widetilde{T}_l) \left.\frac{\partial q_s}{\partial \widetilde{T}_l}\right|_{\widetilde{T}_l = \widetilde{T}} + O\left(\Delta \widetilde{T}_l^{\,2}\right), \tag{55}$$

and the higher order terms are neglected. For ideal gases, the saturation specific humidity is expressed in the saturation vapor pressure as:

$$\widetilde{q}_{sl} = \frac{R_d}{R_v} \frac{e_s}{p - (1 - \frac{R_d}{R_v}) e_s}. \tag{56}$$

By convention, e_s is used to denote the saturation vapor pressure; note however, that e_s is not related to the SFS-TKE $\widetilde{e}$ as defined in section 3.3. The Clausius-Clapeyron relation relates e_s to the temperature:

$$\frac{\mathrm{d}e_s}{\mathrm{d}T} = \frac{L e_s}{R_v T^2}, \tag{57}$$

with $R_v = 461.53 \mathrm{J\ kg^{-1}\ K^{-1}}$ denoting the gas constant for water vapor. It can be solved in very good approximation as:

$$e_s(\widetilde{T}_l) = e_{s0} \exp\left[a \frac{\widetilde{T}_l - T_{\mathrm{trip}}}{\widetilde{T}_l - b}\right], \tag{58}$$

with constants $e_{s0} = 610.78\mathrm{Pa}$, $T_{\mathrm{trip}} = 273.16\mathrm{K}$, $a = 17.27$ and $b = 35.86$. After having substituted in Eqs. 56-58 into the truncated Taylor expansion Eq. 55 we obtain for the saturated specific humidity:

$$\widetilde{q}_s = \widetilde{q}_{sl} \left(1 + \frac{L^2}{R_v c_{p,d} \widetilde{T}_l^{\,2}} \widetilde{q}_t\right) \left(1 + \frac{L^2}{R_v c_{p,d} \widetilde{T}_l^{\,2}} \widetilde{q}_{sl}\right)^{-1}, \tag{59}$$

and finally the cloud water specific humidity can be calculated with Eq. 53. If necessary, the procedure can be applied iteratively to obtain increased accuracy.

3.7.2 SB01 scheme specificities

In a bulk microphysical scheme, one of the most central assumptions to make is on the mass distribution of both the cloud droplets and of the rain droplets. The cloud droplet mass distribution (CDMD) is assumed to be an gamma distribution:

$$n_c(x) = A x^{\nu_c} e^{-Bx} \tag{60}$$

where A and B are input parameters defining the shape of the distribution, depending on q_c, N_c and the width parameter ν_c.

.

The rain drop size distribution (RDSD) is assumed to be a Marshall and Palmer distribution:

$$n_r(r) = N_0 \lambda_r^{\mu_r + 1} r^{\mu_r} e^{-\lambda_r r} \tag{61}$$

with the shape parameter μ_r equal to 0. N_0 and the slope parameter λ_r can be expressed in function of the prognostic variables and μ_r. Note that μ_r has been fixed in the collection parameterizations but can be set to a varying value in order to solve the other processes. For autoconversion and accretion parameterization, correction functions are applied that take

the evolution of the cloud droplet spectra due to conversion of cloud water in rain water into account.

In comparison with the standard Seifert-Beheng scheme, the following modifications are made in the adaptation in DALES:

– The width of the droplet spectrum ν_c is parameterized as a function of q_c (Geoffroy et al., 2009a):

$$\nu_c = 80(\rho q_c)^{0.6} - 0.25 \tag{62}$$

– The shape parameter for the rain water sedimentation μ_r is parameterized following Geoffroy et al. (2009b):

$$\mu_r = 0.008/(\rho q_r)^{0.6} - 1 \tag{63}$$

– The sedimentation flux of the cloud water specific humidity equates to:

$$F_{q_c}^{\mathrm{sec}} = k_{St}\frac{4}{3}\pi\rho_w\, N_c^{-2/3}\, q_c^{5/3}\exp(5\ln(\sigma_{gc})^2) \tag{64}$$

with $\rho_w = 1000\mathrm{kg\,m^{-3}}$, $k_{St} = 1.2\times10^8\mathrm{m^{-1}s^{-1}}$ and σ_{gc} value equal to 1.32 Geoffroy et al. (2009a).

– For the tendency of rain number concentration due to evaporation is (S08),

$$\mathcal{S}_{N_r}^{\mathrm{evr}} = \gamma\frac{\widetilde{N_r}}{\widetilde{q_r}}\mathcal{S}_{q_r}^{\mathrm{evr}}, \tag{65}$$

a value $\gamma = 0.7$ is chosen (Seifert, personal communication).

3.8 Radiation Schemes

The net radiative heating consists of the (downward pointing) radiative flux divergence integrated over all wavelengths ν:

$$\mathcal{S}_{\theta_l}^{\mathrm{rad}} = \int_0^\infty \frac{\partial F^{\mathrm{rad}}(\nu)}{\partial z}\,\mathrm{d}\nu \tag{66}$$

Two approaches towards radiation modeling are implemented in DALES: Fully resolving the radiative transfer, or parameterizing the vertical component of the longwave radiation and of the shortwave radiation through computationally cheap analytic approximations of the Mie theory, that maintain sufficient accuracy for most purposes. In the parameterized radiation scheme, radiative transfer is computed at every single column of the LES model, neglecting horizontal radiative transfer.

3.8.1 3D Radiation

Due to the integration over many wavelengths, running a full radiation code is generally to costly in a tool that lies emphasis on solving the turbulent flow of the ABL, rather than solving the radiative aspects. To reduce the costs, radiative computations can be performed at a coarser spatial or temporal resolution. However, this can introduce biased errors. In DALES the Monte Carlo Spectral Integration (Pincus and Stevens, 2008) is followed, where at each grid point and at each time step the radiative flux is approximated by the radiative flux of one randomly chosen waveband, or even a randomly chosen part of that waveband where all absorption coefficients are similar. For the actual solving of the radiative flux is the radiative transfer model as described by (Fu and Liou, 1992; Fu et al., 1997). This incorporates a parametrization for the cloud water optical properties. To calculate the radiative effects of gasses, a k-distribution is used. Radiative transfer is computed with a δ four-stream solver in both the infrared and solar parts of the spectrum.

3.8.2 Parameterized longwave radiation

For longwave radiation the absorptivity is controled by the liquid water path (LWP),

$$LWP(x,y,z_1,z_2) = \rho_{air}\int_{z_1}^{z_2} q_c(x,y,z)dz, \tag{67}$$

The net longwave radiative flux F_L^{rad} is linked to the liquid water path through an analytic formula,

$$\begin{aligned} F_L^{\mathrm{rad}}(x,y,z) = {} & F(z_{\mathrm{top}})e^{-kLWP(x,y,z,z_{\mathrm{top}})} \\ & + F(0)e^{-kLWP(x,y,0,z)} \end{aligned} \tag{68}$$

where k is the absorption coefficient, and $F(z_{\mathrm{top}})$ and $F(0)$ represent the total net longwave radiative flux divergence at the top of the cloud and the cloud base, respectively.Larson et al. (2007) discuss the validity of this parameterization in detail. They conclude that when the parameterization constants are optimized for individual stratocumulus cases like the ones set up by Duynkerke et al. (1999),Duynkerke et al. (2004), and Stevens et al. (2005), the formula can yield remarkably accurate fluxes and heating rates.

To study the role of longwave radiative cooling on mixed-layer turbulence, but in the absence of latent heat release effects that occur in a real liquid water cloud, one can add a passive scalar field to the model. This so-called "smoke" cloud has an initial concentration set to unity in the boundary layer and zero above (Bretherton et al., 1999b). The liquid water path in the longwave radiation Eq. 68 is then replaced by the smoke path, which can be computed by substituting q_c by the smoke concentration s in Eq. 67. For a smoke absorptivity $k = 0.02\mathrm{m^2\,kg^{-1}}$ one obtains similar cooling rates as in stratocumulus (Bretherton et al., 1999b). It should be noted that unlike liquid water, smoke is a conserved quantity.

This means that if smoke is transported by turbulence into the inversion layer, it will cause a local cooling tendency in this layer.

3.8.3 Parameterized shortwave radiation

In the shortwave band the cloud optical depth τ is the most important parameter defining the radiative properties of clouds,

$$\tau(x,y,z) = \frac{3}{2}\frac{LWP(x,y,z,z_t)}{r_e \rho_w}. \tag{69}$$

Here r_e defines the cloud droplet effective radius, i.e. the ratio of the third moment tothe second moment of the droplet size distribution (Stephens, 1984). Although r_e depends on the height in the cloud layer and has a maximum value at the top of the cloud, a constant value is used. A typical number for marine boundary layer clouds is $r_e = 10\mu m$, which was observed for stratocumulus over the Pacific Ocean off the coast of California during FIRE I (Duda et al., 1991).

Cloud droplets scatter most of the incident radiation into the forward direction. This asymmetry in the distribution of the scattering angle is measured by the first moment of the phase function, and is commonly refered to as the asymmetry factor g which is taken $g = 0.85$. The radiative transfer for shortwave radiation in clouds is modeled by the delta-Eddington approximation (Joseph et al., 1976). In this approach the highly asymmetric phase function is approximated by a Dirac delta function and a two term expansion of the phase function.

The ratio of the scattering coefficient Q_s to the extinction coefficient Q_e is called the single scattering albedo $\omega_0 = Q_s/Q_e$, and is unity for a non-absorbing medium. Following Fouquart (1985),

$$\omega_0 = 1 - 9\times10^{-4} - 2.75\times10^{-3}(\mu_0+1)e^{-0.09\tau_t}, \tag{70}$$

with τ_t the total optical depth in a subcloud column. Although this expression gives single scattering albedos that are very close to unity, absorption in boundary layer clouds can not be neglected due to the large number of scattering events.

The delta-Eddington equations are exactly the same as the Eddington equations (Joseph et al., 1976) with transformed asymmetry factor g, single-scattering albedo ω_0 and optical depth τ:

$$g' = \frac{g}{1+g} \tag{71}$$

$$\omega_0' = \frac{(1-g^2)\omega_0}{1-\omega_0 g^2} \tag{72}$$

$$\tau' = (1-\omega_0 g^2)\tau \tag{73}$$

For constant ω_0 and g the delta-Eddington equation can be solved analytically (Shettle and Weinman, 1970; Joseph et al., 1976):

$$F_s^{\mathrm{rad}}(x,y,z) = F_0\frac{4}{3}\left[p(C_1 e^{-k\tau'(x,y,z)} - C_2 e^{k\tau'(x,y,z)}) - \beta e^{-\frac{\tau'(x,y,z)}{\mu_0}}\right] + \mu_0 F_0 e^{-\frac{\tau'(x,y,z)}{\mu_0}} \tag{74}$$

with:

$$k = [3(1-\omega_0')(1-\omega_0' g')]^{1/2}, \tag{75}$$

$$p = \left(\frac{3(1-\omega_0')}{1-\omega_0' g'}\right)^{1/2}, \tag{76}$$

$$\beta = 3\omega_0'\mu_0\frac{1+3g'(1-\omega_0')\mu_0^2}{4(1-k^2\mu_0^2)}, \tag{77}$$

and $\mu_0 = \cos\alpha_0$ for a solar zenith angle α_0. The values of the constants C_1 and C_2 in Eq. 74 are calculated from the boundary conditions. A prescribed value for the total downward solar radiation (parallel to the beam) determines the upper boundary condition at the top of the cloud F_0. In addition, it is assumed that at the ground surface a fraction of the downward radiation reaching is reflected back by a Lambertian ground surface with albedo A_g. See for further details Shettle and Weinman (1970) and Joseph et al. (1976). The delta-Eddington solution is applied in every column using the local cloud optical depth. A study by De Roode and Los (2008) on the cloud albedo bias effect showed a good agreement between results obtained with the delta-Eddington approach and from the I3RC Monte-Carlo model (Cahalan et al., 2005) that utilizes the full three-dimensional structure of the cloud field.

3.9 Other forcings and sources

Large-scale forcings, such as the mean geostrophic wind $\boldsymbol{u_g}$, the large-scale subsidence w_s, and the horizontal advective scalar transport can be applied through forcings and sources that can be dependent on height and time. The effects of large-scale subsidence are enforced on the slab-averaged scalar profiles through a prescribed subsidence velocity $w_s(z,t)$:

$$\mathcal{S}_\varphi^{\mathrm{subs}} = -w_s\frac{\partial\langle\widetilde{\varphi}\rangle}{\partial z} \tag{78}$$

Optionally, the slab-averaged prognostic variables can be nudged with a relaxation time scale t^{rel} to a prescribed (time depending) value φ^{rel}:

$$\mathcal{S}_\varphi^{\mathrm{rel}} = -\frac{1}{t^{\mathrm{rel}}}\left(\langle\varphi\rangle - \varphi^{\mathrm{rel}}\right), \tag{79}$$

analogous to large-scale forcings in single column models. The application of $\mathcal{S}_\varphi^{\mathrm{rel}}$ to the horizontal mean $\langle\varphi\rangle$, instead of to the individual values of φ, ensures that room for variability within the LES domain remains, and the small-scale turbulence will not be disturbed by the nudging.

3.10 Code modifications for slope flow

To simulate flow over a sloped surface under an angle α (> 0), a coordinate transformation is performed; computations are then done in a system (s, y, n) , with s and n are the coordinates along and perpendicular to the slope, respectively. Under the assumption that the flow can be considered homogeneous along the slope (see section 4.5), only the buoyancy force is directly dependent on s. To account for this, an additional forcing is introduced:

$$\mathcal{F}_{u_s}^{\text{slope}} = -\frac{g}{\theta_0}(\theta_v - \theta_0)\sin\alpha \tag{80}$$

$$\mathcal{F}_{u_n}^{\text{slope}} = \frac{g}{\theta_0}(\theta_v - \theta_0)(\cos\alpha - 1) \tag{81}$$

To accommodate the periodic horizontal boundary conditions for slope flow, we follow Schumann (1990) in splitting each scalar field φ in an ambient component φ_a that incorporates the z dependency of the mean state, and a deviation φ_d with respect to φ_a.

$$\varphi = \varphi_a + \varphi_d \tag{82}$$

Given a mean height depending profile $\Phi(z)$,

$$\varphi_a = (n\cos\alpha - s\sin\alpha)\Phi(z). \tag{83}$$

The deviation φ_d is now homogeneous in the horizontal direction, and periodic boundary conditions can be applied on it. Currently, this splitting procedure is only implemented in DALES for the liquid potential temperature θ_l, focussing slope flow studies exclusively on the dry boundary layer for now.

3.11 Chemically reactive scalars

DALES is equipped with the necessary tools to study the dispersion of atmospheric compounds using the Eulerian and Lagrangian framework and their chemical transformation. The Lagrangian framework is explained in section 3.12.2. In the Eulerian approach, a line or surface source of a passive or a reactant is included to mimic the emission of an atmospheric compound in the ABL flow allowing the calculation and analysis of the diagnostic scalar fields (Nieuwstadt and de Valk, 1987). If the atmospheric compounds react, the source or sink term in Eq. 7 needs to be included in the numerical calculation. For a generic compound φ_l, this reaction term reads:

$$\mathcal{S}_{\varphi_l} = \mathcal{P}(t, \varphi_m) - \mathcal{L}(t, \varphi_m)\varphi_l \qquad m = 1, ..., n. \tag{84}$$

The resepective terms $\mathcal{P}(t, \varphi_m)$ and $\mathcal{L}(t, \varphi_m)$ are nonnegative and represent production and loss terms for atmospheric compound φ_l reacting on time t with the n species φ_m.

In DALES, we solve the term $\mathcal{S}_{\varphi_l}$ using the chemical solver TWOSTEP extensively described and tested by Verwer (1994) and Verwer and Simpson (1995). In short, this chemical solver is an implicit method with second-order accuracy based on the two-step backward differenation formula. Since in atmospheric chemistry we are delaing with chemical system characterized by a wide range of chemical time scales, *i.e. stiff system of ordinary differential equations*, the two-step solver is able to adjust the time step depending on the chemical reaction rate.

A simple chemical mechanism can serve us as an introduction of the specific form of $\mathcal{P}(t, \varphi_k)$ and $\mathcal{L}(t, \varphi_k)$. Atmospheric chemistry mechanism are composed by first- and second-order reactions. Third-order reactions normally involve water vapour or an air molecule, *i.e.* nitrogen or oxigen. Due to the much larger concentration of these compounds than the reactant concentration, third-order reaction rates are normally expressed as a pseudo second-order reaction, *i.e* $k_{2nd} = k_{3rd}[M]$ where $[M]$ is a molecule of H_2O or air. Therefore, a generic atmospheric chemical mechanism composed by a first- and a second-order reaction reads:

$$a \xrightarrow{j} b + c \tag{R1}$$

$$b + c \xrightarrow{k} a, \tag{R2}$$

where a, b and c are atmospheric compound concentrations, j and k are the first- and second-order reaction rate. For reactant a the $\mathcal{L}$ and $\mathcal{P}$ are resepectively:

$$\mathcal{L} = -j \tag{85}$$

$$\mathcal{P} = kbc. \tag{86}$$

The photodissociation rate j depends on the ultraviolet actinic flux and specific photodissociation properties of the atmospheric compound. Therefore, in DALES j is a function on the diurnal variability (latitude, day of the year) and the presence of clouds. j-values are updated every time step. The cloud influence on the actinic flux is implemented using a function that depends on the cloud optical depth (Eq. 69) (Vilà-Guerau de Arellano et al., 2005). The reaction rate k depends on the absolute temperature, on the water vapor content and the pressure. Depending on the reaction, several reaction rate expressions can be specified at DALES. Moreover, The generally very low concentrations of chemical species in the atmosphere allows us to neglect the heating contribution of the reactions on the liquid water potential temperature $\widetilde{\theta_l}$, or on the water content $\widetilde{q_t}$ and $\widetilde{q_r}$.

For the chemical solver, it is essential that the concentration of the species is nonnegative. Therefore, the entire numerical discretization for the reactants, spatial and temporal integration of advection and diffusion and temporal integration of the chemistry, has to satisfy the following three numerical properties: it has to be conservative, monotone and positive defined. Of the advection schemes that are implemented in DALES, the kappa scheme is best suited to enforce monotonicy and positivity.

The chemistry module is designed to be very flexible in order to allow study of different chemical mechanisms. Required input parameters include the number of inert scalars,

and of chemical species, their initial vertical profiles and surface fluxes, and a list of chemical reactions, together with the reaction rate functions. More information on the chemistry module can be found at Vilà-Guerau de Arellano et al. (2005) and Vilà-Guerau de Arellano et al. (2009).

3.12 Statistics

In DALES, standard output includes time series and slab-averaged profiles of the main variables, the (co-) variances, and of the resolved and SFS-modeled fluxes. The modular set-up of the code facilitates inclusion of many other statistical routines, specifically aimed at the purposes of a particular research question. Sharing such code with the community leaves the code base with a rich pallet of statistics, including specific routines that focus on the details of, for example, radiation, cloud microphysics, or the surface layer. Although not exhaustive, a few examples of the statistical capabilities of DALES are given below.

3.12.1 Conditional sampling

Conditionally averaged profiles can be found by defining a mask M, which is equal to 1 or 0, depending on whether a set condition is true or false, respectively. Popular versions of such conditions are, for instance, clouds ($q_l > 0$), areas of updrafts ($\widetilde{w} > 0$), areas of positive buoyancy ($\theta_v > 0$), and any combination of these conditions. New definitions of the mask M are possible with small adjustments of the code.

3.12.2 Lagrangian statistics

While the Eulerian formulation of the LES favors a Eulerian frame of reference for statistics, many problems can greatly benefit from a Lagrangian point of view. This holds in particular for studies of entrainment and detrainment, since these problems can often be stated as a study on the past and the future of a parcel of in-cloud air. To this end a Lagrangian Particle Dispersion Model (LPDM) has been implemented into DALES. Within this module, massless particles move along with the flow. Since each of the particles is uniquely identifiable, the origins and headings of the particles (and of the air) can be captured.

The position of a particle $\boldsymbol{x}_p$ is determined using:

$$\frac{dx_{i,p}}{dt} = \widetilde{u}_i(\boldsymbol{x}_p; t) + u_i'(\boldsymbol{x}_p; t), \tag{87}$$

where $\widetilde{\boldsymbol{u}}$ is the LES-resolved velocity linearly interpolated to the particle position, and $\boldsymbol{u'}$ is an additional random term that represents the SFS-velocity contribution. This term is especially important in regions where the SFS-TKE is relatively large, such as near the surface or in the inversion zone. The calculation of $\boldsymbol{u'}$ follows Weil et al. (2004), and was tailored for use in LES with TKE-closure. It is implemented in DALES as follows:

$$\begin{aligned} du_i' = &-\frac{3 f_s C_0 \varepsilon u_i'}{4e} dt + \frac{1}{2}\left(\frac{u_i'}{e}\frac{de}{dt} + \frac{2}{3}\frac{\partial e}{\partial x_i}\right) dt \\ &+ (f_s C_0 \varepsilon)^{1/2} d\xi_i. \end{aligned} \tag{88}$$

C_0 is the Langevin-model constant Thomson (1987) and has been set to 6; f_s is the slab-averaged ratio between SFS-TKE and total TKE. $d\xi$ is a Gaussian noise to mimic the velocity field associated with the subfilter turbulence.

Boundary conditions are periodic in the horizontal directions, and emulate the LES boundary conditions at the top and bottom of the domain. Particles are reflected (w_p changes sign) should they hit the top or bottom. For time integration, the third order Runge Kutta scheme is again used, but a significant dependency on the choice of the time integration scheme has not been observed. The LPDM was validated by Heus et al. (2008) for a cumulus topped boundary layer and additionally by Verzijlbergh et al. (2009) for a variety of clear and cloud-topped boundary layers.

3.12.3 Transport, tendencies and turbulence

To study the mechanisms behind the development of the ABL, tendency statistics are included that diagnose slab average profiles of every forcing and source term in Eqs. 6 and 7. Where necessary, the individual terms of the underlying equations can also be diagnosed, such as for the SFS-TKE, radiation or microphysical components. Fluxes and co-variances of the main variables are also calculated.

For a full understanding of the turbulence in the boundary layer,a key quantity is the budget of the total turbulent kinetic energy E:

$$\begin{aligned} \left\langle \frac{\partial E}{\partial t} \right\rangle &= \left\langle \frac{\partial}{\partial t}\left[\frac{1}{2}\left(\widetilde{u}^2 + \widetilde{v}^2 + \widetilde{w}^2\right) + e\right]\right\rangle \\ &= -\left[\langle \widetilde{u}\widetilde{w}\rangle \frac{\partial \langle \widetilde{u}\rangle}{\partial z} + \langle \widetilde{v}\widetilde{w}\rangle \frac{\partial \langle \widetilde{v}\rangle}{\partial z}\right] + \frac{g}{\theta_0}\langle \widetilde{w}\theta_v\rangle \\ &\quad - \frac{\partial \langle \widetilde{w}E\rangle}{\partial z} - \frac{1}{\rho_0}\frac{\partial \langle \widetilde{w}\widetilde{p}\rangle}{\partial z} - \varepsilon \end{aligned} \tag{89}$$

in absence of other forcings. Due to the staggered grid used in DALES each variable entering in the budget terms is evaluated at a different position. In order to correctly build up the different terms, several interpolations have to be performed, which have to be consistent with the used advection scheme and all interpolation details in the prognostic part of the code. A residual term in the budget of E is then unavoidable, although it should be smaller than the physical terms (see Fig. 4 for the budget of E in a sheared CBL). In order to further reduce this residual term, a new method based on Gao et al. (1994) is in development.

4 Applications and Evaluation of DALES

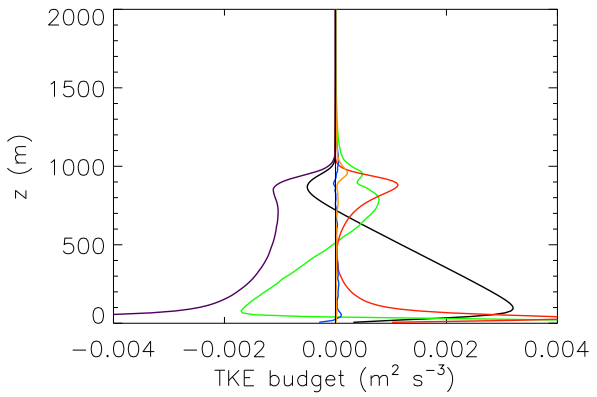

Fig. 4. Vertical profile of the various terms of the total TKE budget in a sheared CBL: total tendency (orange), buoyancy (black), dissipation (violet), transport and pressure (green), shear (red), and the residual (blue).

4.1 Dry Boundary Layers

4.1.1 Convective Boundary Layer

One of the most elementary test-cases for an atmospheric LES is the dry convective boundary layer (CBL). In a CBL a positive heat flux at the surface destabilizes the air resulting in a vigorous turbulence which mixes (thermo)dynamic quantities like heat and momentum over the entire depth of the boundary layer, and which comprises eddies that vary over a wide range of scales, i.e. from the depth of the boundary layer (∼km) down to the Kolmogorov-scale (∼mm). But because the largest scales of motion control most of the vertical transport (e.g. the vertical fluxes of heat and momentum), it is reasonable to fully resolve the large scales on a resolution of $\sim 10-100$m, and account for the scales of motion smaller than the grid scale using the subgrid model (such as Eq. 29).

Probably the most defining feature of a CBL is the fact that the mixed-layer is not confined by a rigid lid (such as Rayleigh-Benard convection), but that it is capped by an inversion, a sudden strong increase of the potential temperature. As such the mixed-layer depth z_i is not fixed, but grows in time: thermals impinging on the inversion cause overlying free tropospheric air to be entrained into the mixed-layer, the depth of which therefore increases. The rate of growth is called the entrainment rate w_e, a key unknown in weather, climate and air quality models. Large-Eddy Simulation provides a powerful tool to make a comprehensive study of entrainment (see e.g. Sullivan et al. (1998); Fedorovich et al. (2004a)) and investigate the dependencies on for example the inversion jump $\Delta\theta_v$, the surface heat flux Q and the actual mixed-layer depth $z_i(t)$. Rather than studying the entrainment rate directly, one can also focus on the entrainment *flux* of heat, in particular the value of the heat flux at the inversion. This approach is followed below for DALES.

Case	Q K m s^{-1}	$d\langle\theta_v\rangle/dz$ K m^{-1}	$z_i(0)$ m	$\Delta\theta_v(0)$ K	z_i m	w_* m s^{-1}
W06	0.06	0.003	750	0	1230	1.34
S024	0.24	0.003	950	8	1096	2.05

Table 3. Simulation details of the two simulated CBLs: weak inversion case (W06) and strong inversion case (S24). $z_i(0)$ and $\Delta\theta(0)$ denote the initial mixed-layer depth and initial temperature jump, respectively.

To test the performance of DALES for dry convective boundary layers, we simulated two of the cases studied by Sullivan et al. (1998), one with a weak inversion $\Delta\theta_v \sim 0.5$K (their case number W06), and one with a strong inversion $\Delta\theta_v \sim 5$K (case S24). The corresponding surface heat flux, initial mixed-layer depth $z_i(0)$ and stratification $d\langle\theta_v\rangle/dz$ of the overlying layer, are given in Tab. 3. In both cases there is no mean wind and hence no (mean) shear. Note that W06 was initiated without an inversion jump. For S24 the initial inversion thickness amounted to 120m (linear interpolation between 300K and 308K over 120m). Both simulations were conducted on a grid of $N_x = N_y = 64, N_z = 96$, using the same resolution as in the original simulations, $\Delta x = \Delta y = 100$m, $\Delta z = 20$m. Time-step was variable, and for the advection of all variables the fifth-order scheme (see section 3.6) was chosen.

In Fig. 5 we present the results averaged from hour 3 to 4. Turbulence statistics are normalized using the convective velocity scale

$$w_* = \left(\frac{g}{\Theta_0} Q z_i\right)^{1/3}$$

where Q is the surface heat-flux in K m/s, and z_i the actual depth of the mixed layer (see Tab. 3). The figures are formatted such that they can be directly compared with the original study by Sullivan et al. (1998). Although W06 was initiated without an inversion, the CBL dynamics is such that it creates its own inversion, as can be seen in Fig. 5a showing the characteristic 'steepening' of the temperature profile in the entrainment zone. The strength of the resulting inversion is the same as observed by Sullivan et al. (1998). The same holds for case S24 (Fig. 5d). For both cases also the normalized heat flux profiles display the usual negative value of roughly -0.2 in the entrainment zone, indicative of the entrainment process (Figs. 5b,e). The sub-grid contribution to the heat flux is rather small in the mixed-layer and near the inversion. The sub-grid contribution to tke, on the other hand, extends over the entire layer (Figs. 5c,f); again the magnitude and shape of the SFS-TKE are in very good agreement with the results reported by Sullivan et al. (1998).

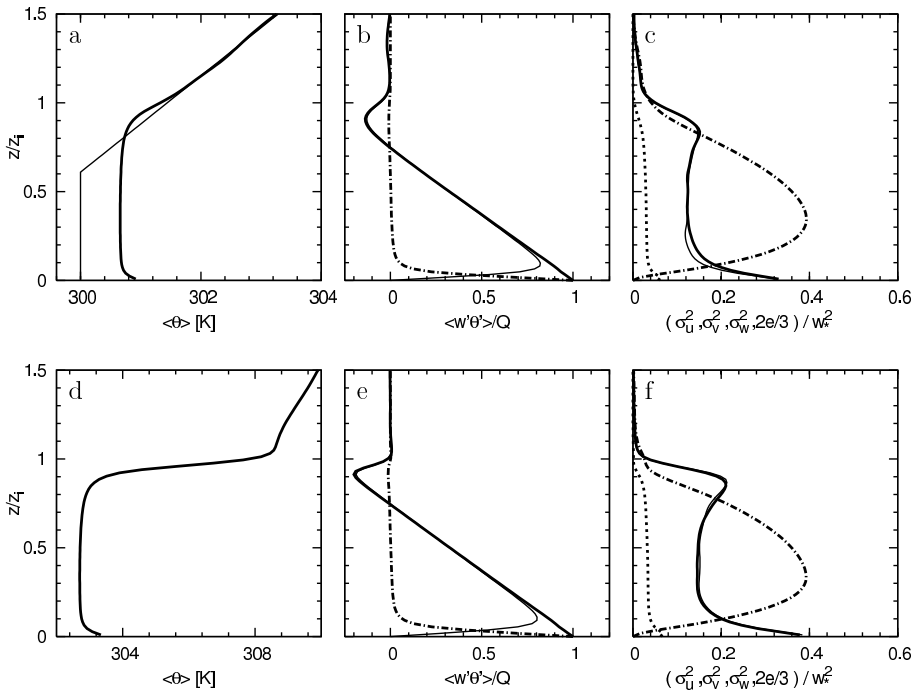

Fig. 5. DALES results for a CBL with a weak inversion (a,b,c) and with a strong inversion (d,e,f), reproducing cases W06 and S24 of the study by Sullivan et al. (1998). For extra information see Tab. 3. All results are averages over hour 3-4. a,d: average temperature profile (thin line in a shows the initial temperature profile). b,e: normalized heat-flux profiles, resolved (thin line), subgrid (dashed) and total (solid line). c,f: turbulence statistics, $\sigma_u^2 = \overline{u'^2}$ (solid line), σ_v^2 (thin line), σ_w^2 (dashed line), and subgrid contribution (dotted line).

4.1.2 Sheared convective boundary layer

To analyze the influence of wind-shear characteristics on the evolution of the CBL, long simulations and large domains are necessary to fulfill a quasy–stationarity flow pattern that matches with the prescribed surface fluxes, and to resolve the expected pattern for forced convection (Khanna and Brasseur, 1998). With DALES, resolutions up to $25\mathrm{m}$ and $6\mathrm{m}$ in the horizontal and vertical directions respectively were considered.

The studies of the sheared CBL focus on the influence of the wind shear on the boundary layer growth due to the modification of the entrainment fluxes (Pino et al., 2003); on identification and parameterization of the main physical mechanisms that control the entrainment heat flux (Kim et al., 2006; Pino et al., 2006b); on the role of shear and the inversion strength in the decay of convective turbulence during sunset (Pino et al., 2006a); and most recently on how to parameterize the different terms of the TKE budget by means a first order jump mixed layer model (Pino and Vilà-Guerau de Arellano, 2008). In an intercomparison study of the sheared CBL in different wind regimes by Fedorovich et al. (2004b), a previous version of the model showed larger entrainment fluxes than the other codes in the intercomparison, producing a warmer and dryer boundary layer. In comparison with this older version of DALES, DALES3.2 shows reduced entrainment fluxes, due to the revised numerical scheme (see Fig. 6).

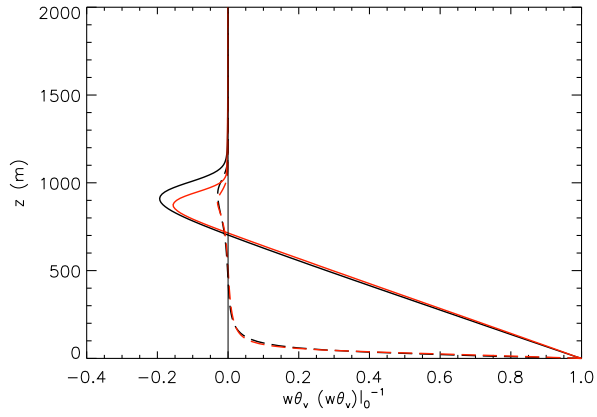

Fig. 6. Vertical profile of the total $\left\langle \widetilde{w}\widetilde{\theta_v} + \widetilde{w'\theta'_v} \right\rangle$ (solid line) and subfilter-scale contribution $\left\langle \widetilde{w'\theta'_v} \right\rangle$ (dashed) of the virtual potential temperature flux obtained after four hours of simulation by DALES2.0 (black) and DALES3.2 (red) with the same physical conditions and advection scheme (2nd order central differences).

Among the results mentioned above we would like to em-

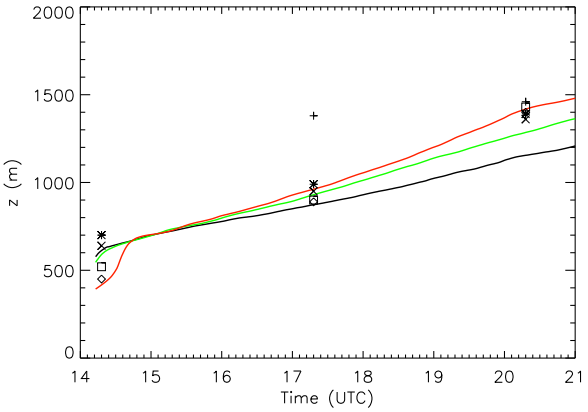

Fig. 7. Boundary layer height z_i observed by radiosondes launched at different facilities of ARM campaign (symbols) and obtained by means of LES: without shear (black), including a constant geostrophic wind of 10 ms^{-1} in the east-west direction (green), and prescribing the observed mean wind (red). Adapted from Pino et al. (2003).

phasize first the influence of the shear in the boundary layer growth by using LES and observations (Pino et al., 2003), and second the influence of the wind shear in the characteristics length scales during afternoon decaying convective turbulence (Pino et al., 2006a). It was shown there that the enhancement of the entrainment heat flux caused by the wind shear at the inversion zone is responsible for an increased boundary layer height. Neglecting this wind shear would results in a significant underestimation in parameterizations of the boundary layer height (see Fig. 7).

4.2 Stable Boundary Layers

In the context of LES, one of the characteristics of stable boundary layers (SBLs) is the mere absence of large eddies (see e.g. the spectra presented in Kaimal and Finnigan (1994)). The stable stratification suppresses vertical motion and transfers turbulent kinetic energy into potential energy. Part of that potential energy is released back as turbulent kinetic energy but part is dissipated through the dissipation of temperature variance. Due to these two aspects, the role of the subfilter-scale model tends to be much larger in LES of SBLs than it is for convective or neutral (but sheared) boundary layers. This implies that for the SBL generally much higher resolutions are used than for other simulations.

The first application of (a previous version of) DALES to stable boundary layers was reported by Galmarini et al. (1998) where a slightly different version of the subfilter-scale model was used.

4.2.1 GABLS

In the context of the GEWEX Atmospheric Boundary Layer Study (GABLS, Holtslag (2006)), a series of model intercomparisons has been organized for SBL cases. In all intercomparisons a single-column model intercomparison case was defined, whereas an LES case was defined in the first and third intercomparison. The first case (Beare et al., 2006) was inspired by the setup of the simulations of Kosović and Curry (2000): an arctic moderately SBL (with $z_i/L \approx 2$, where z_i is the height of the SBL and L the Obukhov length given in Eq. 34). The domain size was set to 400 meter in all three directions. The roughness length z_0 was set to 0.1 m. For heat the same roughness length was applied, and a constant cooling rate of 0.25 K per hour for the surface temperature.

In total 11 models participated in the intercomparison, being run at resolutions from 12.5 m down to 1 m for some models. DALES participated in the intercomparison at resolutions of 12.5 and 6.25 m. For coarse resolutions the subfilter-scale model plays an important role. The results are shown in Fig. 8. The results of DALES are clearly within the range of the other models, although the shear is stronger than in most models close to the surface and weaker at higher levels in the SBL. Furthermore, the strength of the low-level jet seems to be slightly less than in the other models.

4.3 Cloud topped boundary layer

If there is sufficient moisture in the convective boundary so that the total specific humidity q_t exceeds its saturation value q_s, condensation processes will initiate and clouds will start to form. Since q_s increases exponentially with temperature and as temperature decreases with 10 K/km in the convective boundary layer, clouds typically start to form at the top of the convective boundary layer. They are often referred to as boundary layer clouds, as long as the capping inversion at the top of the boundary layer is strong enough to encapsulate them. As a result they have a limited vertical extend of around 3 km which makes the use of LES as a virtual laboratory highly suitable to study the dynamics of boundary layer clouds.

Stratocumulus and shallow cumulus are the two main types of boundary layer clouds that have been simulated extensively in the past with DALES and the schematics of these different types of boundary clouds are depicted in Fig. 9.

Stratocumulus clouds are low-lying, stratiform clouds often covering the sky completely, with a thickness of only several hundreds of meters, capped by a strong inversion. The turbulence that maintains the well-mixed profiles of the conserved variables q_t and θ_l is mainly driven from the top of the stratocumulus deck due the longwave radiative cooling in addition to local cooling and heating due to condensation and evaporation of cloud droplets.

In contrast, shallow cumulus clouds occur as a population of separated small cauliflower shaped clouds with a cloud

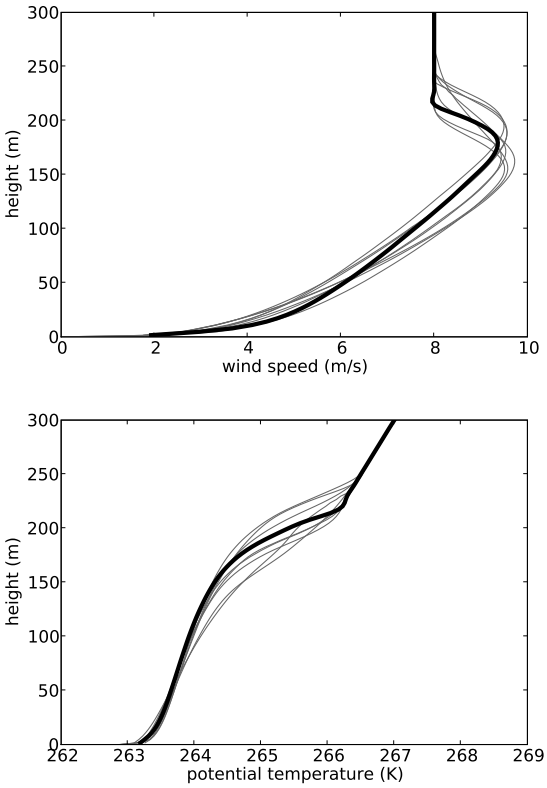

Fig. 8. Profiles of mean wind speed (top) and potential temperature (bottom) for the first GABLS1 LES intercomparison (average over 9th hour of simulation). Solid black line: DALES result at $3.125\mathrm{m}$ resolution and $c_f = 2.0$; grey lines: results of other participants at 3.125 resolution.

base height at around 1 km and a maximum vertical extend of around 2 km. These clouds generally only cover 10 to 30% of the sky. Shallow cumulus clouds usually form on top of the dry rising thermals in the subcloud layer and are dynamically characterized by strong vertical motions due to the condensational heating resulting in inner cloud cores that are positively buoyant with respect to the (dry) environment. As a result the stratification of the mean profile of $\langle\theta_v\rangle$ is stable with respect to vertical displacements of unsaturated test parcels and unstable with respect to saturated test parcels. This effect, often referred to as conditional instability, has no counterpart in any other part of convection and is responsible for the strong intermittant behaviour of cumulus updrafts.

Although stratocumulus might appear, due to its well-mixed character, conceptuallly simpler than shallow cumulus, it is actually harder to simulate stratocumulus clouds in an LES model than to simulate shallow cumulus clouds. This is due to the strong inversion at the top of the stratocumulus deck, where temperature jumps of $10\mathrm{K}$ over $100\mathrm{m}$ are not uncommon. Such strong inversions result from the radiative cooling and are difficult to resolve with LES techniques, re-

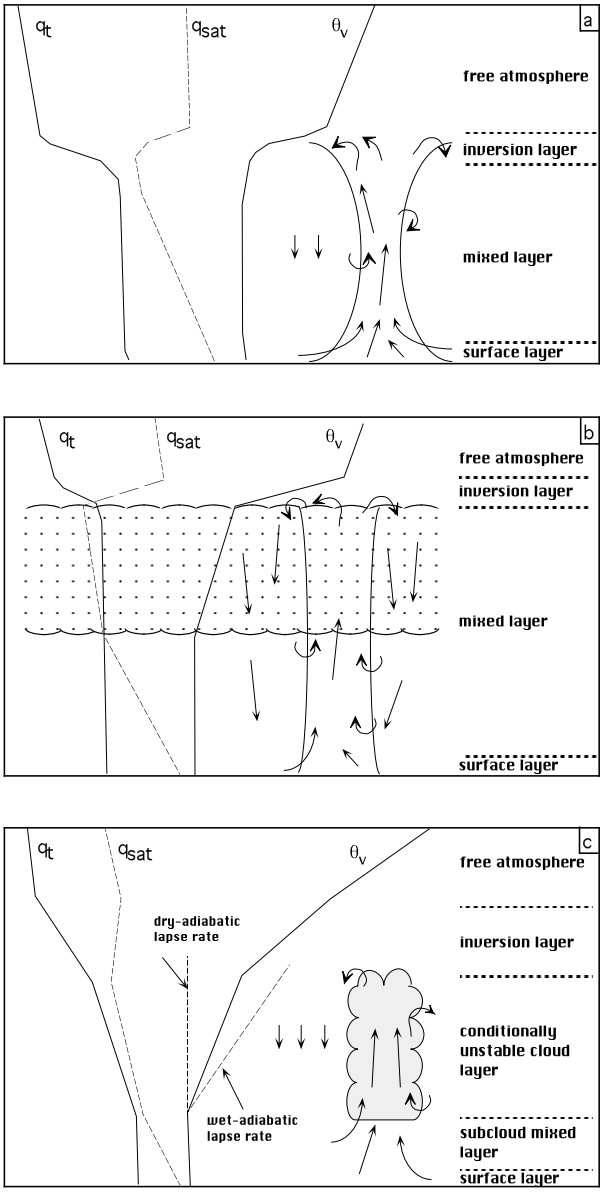

Fig. 9. Schematic overview of the diffferent types of boundary layer clouds.

sulting in unwanted numerical diffusion over this interface which can dominate the transport over the inversion interface. On the other hand, in the case of shallow cumulus clouds the interaction with the radiation is not so strong due to the low cloud fraction. As a result, shallow cumulus clouds are not topped by such strong inversions which simplifies the numerical simulations. Another related simplifying factor is that because of the low cloud fraction the interaction between the clouds and the radiation is not so critical that an interactive treatment of both processes would be essential.

DALES has participated in numerous LES intercomparison studies organized over the last 15 years by the GEWEX Cloud System Studies (GCSS). These intercomparison studies have been set up to serve several purposes. It provides a critical evaluations of the participating LES codes and moreover it provides unique data sets to obtain further insights in the dynamics of the cloud topped boundary layer. More specifically these LES data sets have helped in improving the parameterized formulation of these processes in large scale Numerical Weather Prediction (NWP) and Climate models. In the coming 2 subsections examples are presented how research with DALES have contributed to the improved knowledge of the physics and dynamics of shallow cumulus and stratocumulus.

4.3.1 Stratocumulus

One of the most critical phenomena in the dynamics of stratocumulus is the entrainment of dry air at the top of the cloud layer. Following the flux-jump relation (Stull, 1988), the entrainment rate (w_e) determines the turbulent flux at the top of the boundary layer ($\left\langle \widetilde{w'\varphi'} \right\rangle_e$),

$$\left\langle \widetilde{w'\varphi'} \right\rangle_e = -w_e \Delta \langle \varphi \rangle \tag{90}$$

with $\Delta \langle \varphi \rangle$ the jump across the inversion. This equation is valid for an infinitesimally thin inversion layer and shows the importance of the entrainment rate on the turbulent fluxes at the top of the boundary layer. The representation of turbulent transport by an LES model therefore critically depends on its capability to produce realistic entrainment rates.

Fig. 10 shows the modeled entrainment rates by DALES and by other models as reported by intercomparison studies discussed in detail by Duynkerke et al. (1999), Duynkerke et al. (2004), Stevens et al. (2005) and Ackerman et al. (2009). We find for the ASTEX and FIRE I cases that the entrainment rates from DALES are relatively large in comparison to the other model results. Due to the large measurement errors in the entrainment rates it is not possible to disqualify any model. For the FIRE I case there appears to be a good agreement in the modeled entrainment rates. However, on time scales on the order of a day, relatively small differences in the entrainment rate on the order of $1\mathrm{mm\ s^{-1}}$ can lead to a factor of two difference in the liquid water path (Duynkerke et al., 2004).

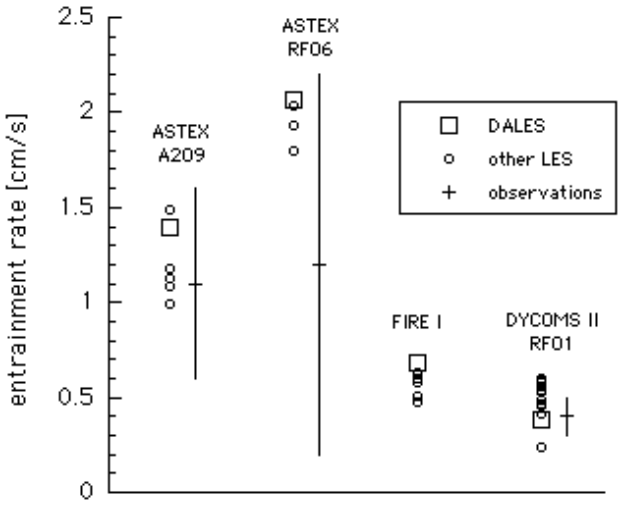

Fig. 10. Entrainment rates from LES models and observations with their errors. The LES results were computed from the third and fourth hour of the simulation. The results of DALES are indicated by the '□' symbol, and the '○' symbol represent results from other LES models.

If we neglect the contribution of the wind-shear term to the TKE budget, and because the vertical integrals of the transport terms vanish, the vertical integrals of the buoyancy and dissipation must balance. Larger entrainment rates cause more negative buoyancy fluxes at the top of the boundary layer, and therefore smaller (absolute) values for the vertical integrals for both the buoyancy flux and the dissipation. The DALES results shown in the figure were all obtained with the numerically dissipative kappa advection scheme. It is therefore remarkable that running these stratocumulus cases with the central difference scheme, which conserves variance, gives a *larger* bulk dissipation and smaller entrainment rates than with the kappa scheme.

The small entrainment rate simulated by DALES for the DYCOMS II stratocumulus case can be explained by a strong reduction of the longwave radiative cooling term after a rapid cloud break-up and a near transition to a clear convective boundary layer during the first two hours of the simulation. Note that according to the observations the cloud deck did not thin. It should be noted that for the DYCOMS II case entrainment of relatively dry and warm air leads to buoyancy reversal. This means that evaporative cooling is sufficiently strong to cause negatively buoyant mixed parcels near cloud top. In LES models the negatively buoyant parcels sink and generate TKE that supports more entrainment and the formation of negatively buoyant parcels. This positive feedback is in accord with the theoretical consideration of Randall (1980) and Deardorff (1980), but appears to be too strong in the model, in particular with the kappa scheme. Stevens et al. (2005) discuss that in the buoyancy reversal regime, LES re-

sults become very dependent on the details of the subfilter-scale model and numerical scheme. The obvious disagreement between the evolution of the observed cloud deck and the LES results calls for further study.

4.3.2 Shallow Cumulus

A number of interesting and well-documented shallow cumulus cases based on observational studies have been simulated by DALES over the last 10 years. These studies include: non-precipitating steady-state marine shallow cumulus based on the Barbados Oceanographic and Meteorological Experiment (BOMEX) (Siebesma et al., 2003) and on the Atlantic Trade Wind Experiment (ATEX) (Stevens et al., 2001), diurnal cycles of shallow cumulus over land observed on June 21, 1997 at the Southern Great Plains (SGP) site (Brown et al., 2002) and during the Small Cumulus Microphysics Study (SCMS) (Neggers et al., 2003a) and more recently precipitating marine shallow cumulus (van Zanten et al., 2009) such as observed during the Rain in Cumulus over the Ocean (RICO) field study Rauber et al. (2007). All these cases have been used to critically evaluate the DALES results against observations and to help developing and testing theories, conceptual models and parameterizations of shallow cumulus convection. In this section we will give a short overview of the results of these studies.

The first category of these studies is related to cloud geometrical issues. In Siebesma and Jonker (2000) it has been shown that the simulated cumulus cloud boundaries have self-similar or fractal properties that can be characterized by a fractal dimension $D_f = 7/3$. These results are in excellent agreement with observational studies and therefore provide a critical test of the capability of DALES to simulate realistic cumulus clouds. Moreover, these results helped in constructing theoretical scaling arguments explaining why cloud boundaries choose to be self-similar with a dimension of $7/3$. Another intriguing cloud geometrical topic is related to the question: what is the shape of the cumulus cloud size distribution? It is well known that shallow cumulus cloud ensembles consist of many small clouds and lesser large clouds but the precise shape of the cloud size distribution is still an open issue. Extensive numerical studies with DALES show that the cloud size density of the simulated cloud populations is described well by a power-law from scales smaller than the standard grid-spacing (50m) up to scales of typically 1000m with a power-law exponent of -1.70 (Neggers et al., 2003b). This exponent is comparable to values found in observational studies (Cahalan and Joseph, 1989; Rodts et al., 2003). No convincing theory for the powerlaw behaviour nor for the scale break has yet been put forward. Finally, more recently analyses with DALES of up- and downdrafts in and around individual cumulus clouds have shown that strong updrafts in individual cumulus clouds are typically surrounded by so-called subsiding shells with persistent downdrafts (Heus and Jonker, 2008). These downdrafts are driven by negative buoyant forces that result from the evaporative cooling of the cloud water. As they surround the clouds along their entire perimeter, the subsiding shells cover a significant area and are therefore found to be responsible for a large part of the downward mass transport (Jonker et al., 2008).

The second category studies is related to transport due to cumulus convection which is one of the important processes that needs parameterization in large scale NWP and climate models. The time evolution of a moist conserved variable φ due to moist convection can be written as

$$\frac{\partial \varphi}{\partial t} = -\frac{\partial F_\varphi}{\partial z} \tag{91}$$

where F_φ is the (upward pointing) turbulent flux. A popular method to parameterize this turbulent flux is through the use of a so called mass flux approach

$$F_\varphi \approx \frac{M}{\rho}(\varphi_c - \langle\varphi\rangle). \tag{92}$$

where ρ is the density and the subscript c refers to cloud averaged values of φ and the mass flux is defined as $M \equiv \rho a_c w_c$ Betts (1975), i.e. essentially the product of the cloud averaged vertical velocity times w_c and the fractional cloud area a_c. Usually a cloud model is derived to obtain equations for M and φ_c

$$\frac{\partial M}{\partial z} = M(\varepsilon - \delta) \tag{93}$$

$$\frac{\partial \varphi_c}{\partial z} = -\varepsilon\,(\varphi_c - \langle\varphi\rangle) \tag{94}$$

Within this cloud model the key variables are the fractional entrainment ε and fractional detrainment δ rate. These inverse length scales are measures of the rate of dilution of the cloud ensemble (entrainment) and the rate of air leaving the cloud ensemble (detrainment) and LES results from DALES have been used extensively to diagnose ε and δ on the basis of Eqs. 93 and 94 (Siebesma and Cuijpers, 1995). This approach has initiated considerable research in developing theories and models of these exchange mechanisms between clouds and environment. From these studies it has become clear that the fractional entrainment rate can be well estimated by the inverse cloud depth (Siebesma et al., 2003). The fractional detrainment rate δ is typically larger than ε as a result of the fact the cloud fraction a_c is in general decreasing with height.

Another useful additional equation often used in cloud models is the vertical velocity equation for the cloud ensemble (Simpson and Wiggert, 1969)

$$\frac{1}{2}\frac{\partial w_c^2}{\partial z} = -b\,\varepsilon_w\,w_c^2 + a\,B \quad \text{with} \quad B = \frac{g}{\theta_0}(\theta_{v,c} - \langle\theta_v\rangle) \tag{95}$$

which describes how buoyancy forces and entrainment processes influence the vertical velocity in the clouds. Adjustable prefactors a and b are introduced in this equation

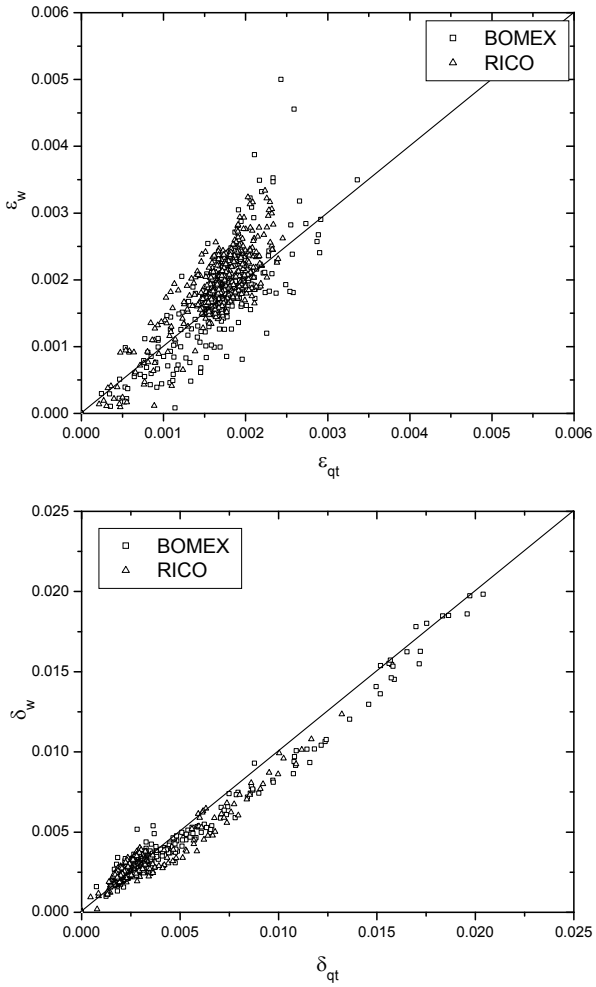

Fig. 11. Comparison of LES derived fractional entrainment and detrainment rates ε_q and δ_q using $\phi = q_t$ based on Eq. 95 (horizontal axis) versus LES estimates of these rates ε_w and δ_w based on the vertical velocity equation Eqs. 96 and 97

.

to incorporate pressure perturbation effects and incloud turbulent effects in an implicit way. By using Eq. 95 and Eq. 93 we can derive alternative expressions for the entrainment that are more linked to the dynamics

$$\varepsilon_w = \left(\frac{B}{w_c^2}\right) - \frac{1}{b}\frac{\partial \ln w_c}{\partial z} + \frac{a}{b} \tag{96}$$

$$\delta_w = \left(\frac{B}{w_c^2}\right) - \frac{(1+b)}{b}\frac{\partial \ln w_c}{\partial z} + \frac{a}{b} - \frac{\partial \ln a_c}{\partial z} \tag{97}$$

In Fig. 11 we compare the entrainment and detrainment rates based on Eqs. 95, 96, and 97 for which estimates of $a = 0.6$ and $b = 1$ are used for a large variety of different LES experiments.

The fact that the results fall reasonably well on the diagonal shows that Eq. 95 and Eqs. 93 are consistent, so that the subscripts of ε_w and δ_w can be removed and Eqs. 96 and 97 can be used as well to interpret the exchange rates. It can also be observed that ε can vary considerably between values of $1 \sim 4 \times 10^{-3}\mathrm{m}^{-3}$ indicating that parameterizations that use a constant value for ε is not a good option. Furthermore it should be noted that the range of variability for δ is much larger $1 \sim 20 \times 10^{-3}\mathrm{m}^{-3}$. More detailed analysis shows that this large variability is mainly due to the gradient of the cloud fraction with height in Eq. 97. This indicates that, in order to have a good estimate of the mass flux M, it is more relevant to have a good parameterisation of δ rather than for ε, a statement already emphasized in de Rooy and Siebesma (2008). In that respect it is surprising to see that most of the research efforts have been concentrated on entrainment rather than on detrainment.

4.4 Heterogeneous surfaces

DALES has contributed to the understanding of flow over thermally heterogeneous terrain. The study of van Heerwaarden and Vilà-Guerau de Arellano (2008) addressed the question whether convective cloud formation is more likely to form over a land surface that has a heterogeneous surface flux compared to a land surface that is homogeneously heated.

Heterogeneous land surfaces were simulated by creating two stripes of 3.2 km wide at the land surface in the model, as this is the spatial scale at which heterogeneity is considered to modify the turbulent structure of the overlying CBL the most. The turbulent fluxes at the land surface were prescribed. Both stripes had the same sum of sensible and latent heat, but a different Bowen ratio. The left stripe was characterized by a small Bowen ratio, whereas the right stripe had a large ratio. In this setup the LES model was run for four hours; statistics were calculated over the last hour.

The main findings of the study are summarized in Fig. 12 that shows the relative humidity in the CBL and the wind vectors in a case where the free atmosphere is moist (left panel) and in a case where the free atmosphere is dry.

In both cases a secondary circulation (see wind vectors) distributes heat and moisture towards the area that has a relatively large sensible and a small latent heat flux. At these hot spots, strong but moist thermals rise, resulting in a large relative humidity over the area that has the smallest latent heat flux. In case of a dry free troposphere (right panel), the secondary circulation can transport very dry free tropospheric air downwards to the land surface. Therefore, a very low relative humidity is found over the area that has the largest latent heat flux.

To conclude, the study showed that heterogeneity results in a situation that is more favorable for cloud formation, regardless of the specific humidity of the free troposphere.

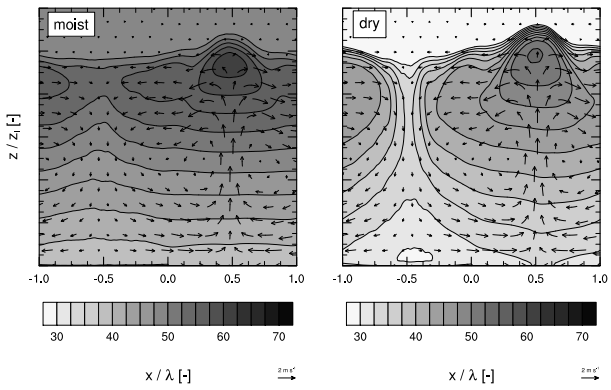

Fig. 12. Cross section of the 1-h-averaged relative humidity $\overline{RH}$ for a case with a moist free troposphere (left) and a case with a dry free troposphere (right). The horizontal coordinates are scaled by the patch size λ and the vertical coordinates are scaled by the CBL height z_i. Vectors indicate the wind direction and magnitude. From van Heerwaarden and Vilà-Guerau de Arellano (2008).

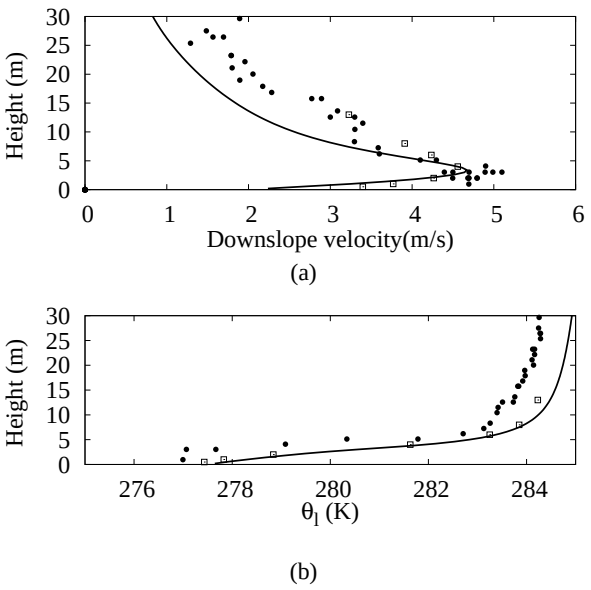

Fig. 13. Mast profiles (squares), balloon data (dots) and LES profiles of downslope velocity (a) and potential temperature (b) in flow over a sloped surface.

4.5 Atmospheric flow over sloping surfaces

Compared with the many successful large-eddy simulations of the boundary layer over flat terrain, as of yet only a few simulations of the ABL over sloping surfaces have been carried out. One of the problems concerning the simulation of slope flow, is that the potential temperature as well as the depth of the flow and the flow velocity change along the slope. Observations of katabatic flow, however, have shown that the flow in a strongly stratified boundary layer and / or over (moderately) steep slopes varies only slightly along the slope (Haiden and Whiteman, 2005). Therefore, although DALES currently only facilitates periodic boundary conditions, we are still able to study homogeneous slope flow. One of the outlooks is to implement open boundary conditions, which would enable the simulation of slope flow under a larger range of circumstances. Nonetheless, DALES has in recent years successfully been used to study homogeneous katabatic flow over moderately steep slopes.

Axelsen and van Dop (2009) performed a model validation by comparing simulation results to observations from two glaciers. They found that the simulated profiles of temperature and downslope velocity were quantitatively in agreement with the observations. An example is given in Fig. 13. Near the surface the downslope velocity increases with height and reaches a maximum at a height of $z \approx 4$ m. Above the wind maximum height, the downslope velocity decreases with height. The figure shows that near the surface the simulated and observed velocity profiles agree, but above the wind maximum the model underestimates the velocity. The profile of the simulated potential temperature is also seen to agree rather well with the mast measurements, but that there is a systematic offset between the balloon measurements and the simulated potential temperature. The agreement between modelled and observed fluxes of momentum and buoyancy were less satisfactory (not shown). However, the observations were influenced by processes such as a valley wind, cross-slope winds, and gravity waves. The latter processes, which enhance the turbulence production and the vertical mixing in the katabatic layer, are not accounted for in the numerical model.

4.6 Dispersion and chemically reacting flows

We summarize here the main research results achieved in the field of turbulent dispersion and chemical transformations using DALES. The plume dispersion main characteristics and statistics under different ABL flow conditions have been thoroughly investigated using DALES. Dosio et al. (2003, 2005) and Dosio and Vilà-Guerau de Arellano (2006) investigated the plume disperion in the dry CBL from a Eulerian and a Lagrangian perspective. Based on DALES results, they derived a parameterization to include the effect of shear on the plume spreading, studied the validity of Taylor's diffusion theory for horizontal and vertical dispersion, and separated the contributions of small- and large-scales on the plume evolution, both from an absolute coordinate system as well as relative to the plume's center of mass. Verzijlbergh et al. (2009) extended this study to determine the influence of stratocumulus and shallow cumulus on the turbulent dispersion properties and related to turbulent structures like skewness of the vertical velocity. As an example, Fig. 14 shows the vertical concentration characteristics and the location of the maximum concentration under different ABL conditions:

dry convective boundary layer, stratocumulus and shallow cumulus Verzijlbergh et al. (2009).

Similarly to turbulent dispersion, the chemical transformations in the ABL are influenced by the characteristics of the turbulent flow. This turbulent control is particularly important when the turbulent time scale (τ_t) and the chemistry time scale (τ_c) have similar values, i.e., the order of magnitude of the Damköhler number (τ_t/τ_c) is $\mathcal{O}(1)$. Under this regime, the species are chemically transformed at a different reaction rate depending on the way species are introduced in the ABL, premixed or non-premixed, and the turbulent intensity to mix chemical species. Key tropospheric chemical reactions involving species such as nitric oxide and certain biogenic hydrocarbons like isoprene are therefore controlled by turbulence.

Following Schumann (1989), Petersen et al. (1999) and Petersen and Holtslag (1999) studied by means of LES how the transport and mixing of reactants in the CBL is influenced by the presence of vigorous thermals and subsidence motions. Based on the DALES results, they suggested a parameterization to represent the fluxes and covariance of reactants in large scale chemistry transport models. The research was extended to study more complex mechanism under non-uniform emissions of the reactants (Krol et al., 2000; Vilà-Guerau de Arellano et al., 2004). To further study the influence of the reactivity on high-order moments, a spectral analysis showed that the reactant variability (variance) depends strongly on the reaction rate (Jonker et al., 2004). The analysis was done using the DALES simulation of a turbulent flow reacting according to the scheme (R1)-(R2). These results showed large variations in the characteristic length scale as a function of the Damköhler number and the state of the chemical equilibrium.

To improve parameterizations in large-scale atmospheric chemistry models, Vinuesa and Vilà-Guerau de Arellano (2003, 2005) proposed an expression of an effective reaction rate (k_{eff}) that takes into account explicitely the influence of turbulent mixing on the reaction rate.

The moist and optically thick boundary layer clouds can also influence atmospheric chemistry. DALES was used to study the combined effect of turbulence and radiation on simple chemical mechanism in a dry smoke cloud (Vilà-Guerau de Arellano and Cuijpers, 2000) and shallow cumulus (Vilà-Guerau de Arellano et al., 2005). Fig. 15 shows the cloud water content and the photostationary state (Φ) in a CBL developed over land characterized by the presence of shallow cumulus. Φ quantifies the effect of the physical processes (turbulence and radiation) on the atmospheric chemistry. For the reactants nitric oxide (NO), ozone ($\mathrm{O_3}$) and nitrogen dioxide ($\mathrm{NO_2}$), it is defined as $\Phi = (k[\mathrm{NO}][\mathrm{O_3}])/(j[\mathrm{NO_2}])$. Departure from the value $\Phi = 1$ indicate perturbations of the chemical equilibrium either by radiation or turbulent processes.

5 Outlook

As was shown in this paper, DALES can provide reliable results for a multitude of atmospheric conditions, and there are many alleys of study that can be pursued with DALESv3.2. In the field of cloudy boundary layers, very fine grid spacing can be used to reliably resolve most of the dynamics within and around the cloud. Simulations on relatively large horizontal domains ($\sim 25\mathrm{km}$) can mimic the physics in an area similar to a single column of a regional or global model. On that scale, LES is well capable of variability studies that are necessary to improve the GCMs, and to study the impact of GCM grid refinement. For other studies, LES can provide spatial and temporal turbulence characteristics that cannot be easily retrieved from measurements alone. This is always a role that LES can play, but it can be especially important in spatially anisotropic or inhomogeneous situtations, such as in the fields of flow over sloped or heterogeneous surfaces.

While there are many plans to use DALES in its current state, ongoing improvement of the code is also planned. In the near future, we aim to be able to run DALES in more diverse and more realistic scenarios than DALES is currently capable of. Furthermore, we aim to focus on studies that makes integrated use of several of the features of DALES.

One possibilty to broaden the applicability of DALES is to study deeper convective systems in LES. To do so, it is necessary to leave the Boussinesq approximation behind, and also to account for solid phase hydrometeors.

Another aspect of more realistic LES, is to better account for the anisotropic turbulence around steep gradients and inversion layers in stable boundary layers, dry convective boundary layers, and stratocumulus layers. Increasing computer power and resolution could resolve these gradients within the coming years, but more intelligent subfilter-scale modeling could also give a significant contribution in solving this problem. This is especially important in critical stratocumulus cases, where entrainment of relatively dry and warm air leads to buoyancy reversal. This means that evaporative cooling is sufficiently strong to cause negatively buoyant mixed parcels near cloud top. In LES models the negatively buoyant parcels sink and generate TKE that supports more entrainment and the formation of negatively buoyant parcels. Stevens et al. (2005) discuss that in the buoyancy reversal regime, LES results become very dependent on the details of the subfilter-scale model and numerical scheme. The obvious disagreement between the evolution of the observed cloud deck and the LES results calls for further study.

To study the interactions between the various components of the model, we strive to have the modules as interactive as possible. This could for instance lead to better understanding of coupling mechanisms between radiative forcings and the surface conditions, coupling between radiation and chemistry, or between chemistry and cloud and aerosol formation.

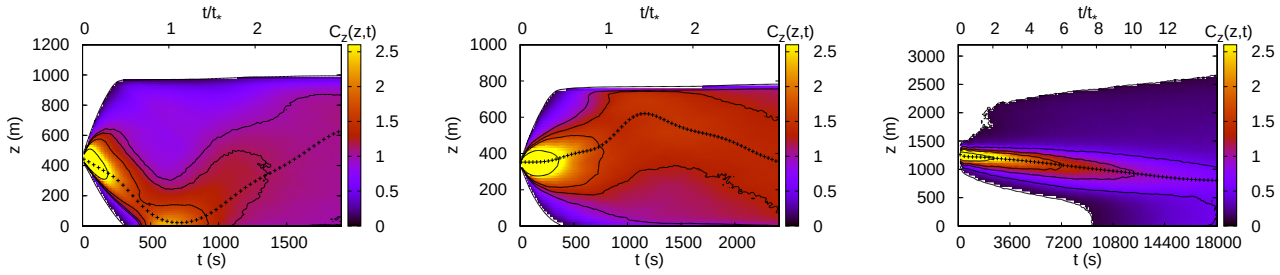

Fig. 14. Evolution on time of the vertical concentration (crosswind integrated) of a plume released under dry convective conditions as a function of the releasing time (dimensional and non-dimensional). Concentration has been multiplied by a factor 1000 to obtain a convenient scale. The crosses indicates the position of the maximum concentration.

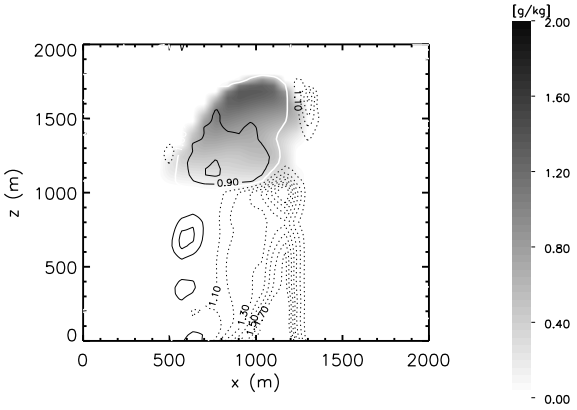

Fig. 15. Instantaneous vertical cross section of the cloud water q_c (g/Kg) content and the photostationary state (Φ) calculated using the NO, NO_2 and O_3 mixing ratios. At chemical equilibrium Φ=1.

Acknowledgements. We thank all contributors to DALES for their work, such as Hans Cuijpers, Mathieu Pourquie, Margreet van Zanten, Alessandro Dosio, and Han van Dop.

References

Ackerman, A., van Zanten, M. C., Stevens, B., Savic-Jovcic, V., Bretherton, C. S., Chlond, A., Golaz, J.-C., Jiang, H., Khairoutdinov, M., Krueger, S. K., Lewellen, D. C., Lock, A., Moeng, C.-H., Nakamura, K., Ovtchinnikov, M., Petters, M. D., Snider, J. R., Weinbrecht, S., and Zulauf, M.: Large-eddy simulations of a drizzling, stratocumulus-topped marine boundary layer, Mon. Wea. Rev., 137, 10831110, doi:10.1175/2008MWR2582.1, 2009.

Axelsen, S. L. and van Dop, H.: Large-Eddy Simulations and observations of slope flow, Acta Geophysica, in preparation, 2009.

Basu, S., Steeneveld, G. J., Holtslag, A. A. M., and Bosveld, F. C.: Large-Eddy Simulation Intercomparison Case Setup for GABLS3, in: 18th Symposium on Boundary Layers and Turbulence, Stockholm, Sweden, 9 - 13 June, 2008. - Boston : American Meteorological Society, - p. - 8A.7., 2008.

Beare, R. J., Macvean, M. K., Holtslag, A. A. M., Cuxart, J., Esau, I., Golaz, J.-C., Jimenez, M. A., Khairoutdinov, M., Kosovic, B., Lewellen, D., Lund, T. S., Lundquist, J. K., Mccabe, A., Moene, A. F., Noh, Y., Raasch, S., and Sullivan, P.: An Intercomparison of Large-Eddy Simulations of the Stable Boundary Layer, Bound.-Layer Meteor., 118, 247–272, doi:10.1007/s10546-004-2820-6, 2006.

Beljaars, A. C. M.: Numerical schemes for parametrizations, in: Proceedings of the ECMWF Seminar on Numerical Methods in Atmospheric Models, pp. 1–42, ECMWF, 1991.

Betts, A. K.: Parametric interpretation of trade-wind cumulus budget studies, J. Atmos. Sci., 32, 1934–1945, doi:10.1175/1520-0469(1975)032⟨1934:PIOTWC⟩2.0.CO;2, 1975.

Bretherton, C. S., Krueger, S. K., Wyant, M. C., Bechtold, P., Meijgaard, E. V., Stevens, B., and Teixeira, J.: A GCSS boundary-layer cloud model intercomparison study of the first ASTEX Lagrangian experiment, Bound.-Layer Meteor., 93, 341–380, doi:10.1023/A:1002005429969, 1999a.

Bretherton, C. S., MacVean, M. K., Bechtold, P., Chlond, A., Cuxart, J., Khairoutdinov, M., Kosovic, B., Lewellen, D. C., Moeng, C.-H., Siebesma, A. P., Stevens, B., Stevens, D. E., I.Sykes, and Wyant, M. C.: An intercomparison radiatively-driven entrainment and turbulence in a smoke cloud, as simulated by different numerical models, Quart. J. Roy. Meteor. Soc., 125, 391–423, doi:10.1002/qj.49712555402, 1999b.

Bretherton, C. S., McCaa, J. R., and Grenier, H.: A new parameterization for shallow cumulus convection and its application to marine subtropical cloud-topped boundary layers. Part I: Description and 1D results, Mon. Wea. Rev., 132, 864–882, doi:10.1175/1520-0493(2004)132⟨0864:ANPFSC⟩2.0.CO;2, 2004.

Brown, A. R., Cederwall, R. T., Chlond, A., Duynkerke, P. G., Golaz, J. C., Khairoutdinov, M., Lewellen, D. C., Lock, A. P., MacVean, M. K., Moeng, C.-H., Neggers, R. A. J., Siebesma, A. P., and Stevens, B.: Large-eddy simulation of the diurnal cy-

cle of shallow cumulus convection over land, Quart. J. Roy. Meteor. Soc., 128, 1075–1093, doi:10.1256/003590002320373210, 2002.

Businger, J. A., Wyngaard, J. C., Izumi, Y., and Bradley, E. F.: Flux-profile relationships in the atmospheric surface layer, J. Atmos. Sci., 28, 181–189, doi:10.1175/1520-0469(1971)028⟨0181:FPRITA⟩2.0.CO;2, 1971.

Cahalan, R. and Joseph, J.: Fractal statistics of cloud fields, Mon. Wea. Rev., 117, 261–272, doi:10.1175/1520-0493(1989)117⟨0261:FSOCF⟩2.0.CO;2, 1989.

Cahalan, R. F., Oreopoulos, L., Marshak, A., Evans, K. F., Davis, A. B., Pincus, R., Yetzer, K. H., Mayer, B., Davies, R., Ackerman, T. P., Barker, H. W., Clothiaux, E. E., Ellingson, R. G., Garay, M. J., Kassianov, E., Kinne, S., Macke, A., O'Hirok, W., Partain, P. T., Prigarin, S. M., Rublev, A. N., Stephens, G. L., Szczap, F., Takara, E. E., Várnai, T., Wen, G., and Zhuravleva, T. B.: The I3RC: Bringing together the most advanced radiative transfer tools for cloudy atmospheres, Bull. Amer. Meteor. Soc., 86, 1275–1293, doi:10.1175/BAMS-86-9-1275, 2005.

Cuijpers, J. W. M.: Subgrid Parameterization in a large-eddy simulation model, in: Ninth Symp. on Turbulence and Diffusion, pp. 176–179, Amer.Meteor.Soc., Roskilde, Denmark, 1990.

Cuijpers, J. W. M. and Duynkerke, P. G.: Large-eddy simulation of trade-wind cumulus clouds, J. Atmos. Sci., 55, 151–162, doi:10.1175/1520-0469(1998)055⟨0151:IOSANE⟩2.0.CO;2, 1993.

de Roode, S. R.: The role of eddy diffusivity profiles on stratocumulus liquid water path biases, Mon. Wea. Rev., 135, 2786–2793, doi:10.1175/MWR3426.1, 2007.

De Roode, S. R. and Los, A.: The effect of temperature and humidity fluctuations on the liquid water path of non-precipitating closed-cell stratocumulus, Quart. J. Roy. Meteorol. Soc, 134, 403–416, doi:10.1002/qj.222, 2008.

de Rooy, W. C. and Siebesma, A. P.: A simple parameterization for detrainment in shallow cumulus, Mon. Wea. Rev., 136, 560–576, doi:10.1175/2007MWR2201.1, 2008.

Deardorff, J. W.: Theoretical expression for the counter-gradient vertical heat flux, J. Geophys. Res., 77, 5900–5904, doi:10.1029/JC077i030p05900, 1972.

Deardorff, J. W.: Three-dimensional numericla modeling of the planetary boundary layer., in: Workshop on Meteorology, edited by Haugen, D. A., pp. 271–311, American Meteorological Society, 1973.

Deardorff, J. W.: Stratocumulus-capped mixed layers derived from a three dimensional model, Bound.-Layer Meteor., 18, 495–527, doi:10.1007/BF00119502, 1980.

Dosio, A. and Vilà-Guerau de Arellano, J.: Statistics of absolute and relative dispersion in the atmospheric convective boundary layer: a Large-Eddy Simulation study, J. Atmos. Sci., 63, 1253–1272, doi:10.1175/JAS3689.1, 2006.

Dosio, A., Vilà-Guerau de Arellano, J., Holtslag, A. A. M., and Builtjes, P. J. H.: Dispersion of a passive tracer in buoyancy- and shear-driven boundary layers., J. Appl. Meteor., 42, 1116–1130, doi:10.1175/1520-0450(2003)042⟨1116:DOAPTI⟩2.0.CO;2, 2003.

Dosio, A., Vilà-Guerau de Arellano, J., Holtslag, A. A. M., and Builtjes, P. J. H.: Relating Eulerian and Lagrangian statistics for the turbulent dispersion in the atmospheric convective boundary layer, J. Atmos. Sci., 62, 1175–1191, doi:10.1175/JAS3393.1, 2005.

Duda, D. P., Stephens, G. L., and Cox, S. K.: Microphysical and radiative properties of marine stratocumulus from tethered balloon measurements, J. Appl. Meteor., 30, 170–186, doi:10.1175/1520-0450(1991)030⟨0170:MARPOM⟩2.0.CO;2, 1991.

Duynkerke, P., Jonker, P., Chlond, A., van Zanten, M., Cuxart, J., Clark, P., Sanchez, E., Martin, G., Lenderink, G., and Teixeira, J.: Intercomparison of three- and one-dimensional model simulations and aircraft observations of stratocumulus, Bound.-Layer Meteor., 92, 453–487, doi:10.1023/A:1002006919256, 1999.

Duynkerke, P. G., de Roode, S. R., et al.: Observations and numerical simulation of the diurnal cycle of the EUROCS stratocumulus case, Quart. J. Roy. Meteor. Soc., 140, 3269–3296, doi:10.1256/qj.03.139, 2004.

Emanuel, K. A.: Atmospheric Convection, Oxford University Press, New York, 1994.

Fedorovich, E., Conzemius, R., and Mironov, D.: Convective entrainment into a shear-free, linearly stratified atmosphere: bulk models reevaluated through large-eddy simulations, J. Atmos. Sci., 61, 281–295, doi:10.1175/1520-0469(2004)061⟨0281:CEIASL⟩2.0.CO;2, 2004a.

Fedorovich, E., R.Conzemius, Esau, I., Chow, F. K., Lewellen, D., Moeng, C.-H., Sullivan, P., Pino, D., and Vilà-Guerau de Arellano, J.: Entrainment Into Sheared Convective Boundary Layers As Predicted By Different Large Eddy Simulation Codes, in: The 16th Symposium on Boundary-Layers and Turbulence, 2004b.

Fouquart, Y.: Radiation in boundary layer clouds, in: Report, JSC/CAS Workshop on Modelling of Cloud-Topped Boundary Layer, pp. Appendix D, 40 pp, Fort Collins, CO, WMO/TD 75, 1985.

Fu, Q. and Liou, K.: On the Correlated k-Distribution Method for Radiative Transfer in Nonhomogenecous Atmospheres, J. Atmos. Sci., 49, 2139–2156, doi:10.1175/1520-0469(1992)049⟨2139:OTCDMF⟩2.0.CO;2, 1992.

Fu, Q., Liou, K. N., Cribb, M. C., Charlock, T. P., and Grossman, A.: Multiple Scattering Parameterization in Thermal Infrared Radiative Transfer, J. Atmos. Sci., 54, 2799–2812, doi:10.1175/1520-0469(1997)054⟨2799:MSPITI%⟩2.0.CO;2, 1997.

Galmarini, S., Beets, C., Duynkerke, P., and Vilà-Guerau de Arellano, J.: Stable Nocturnal Boundary Layers: A Comparison of One-Dimensional and Large-Eddy Simulation Models, Bound.-Layer Meteor., 88, 181–210, doi:10.1023/A:1001158702252, 1998.

Gao, S., Gao, Z., and Voke, P.: Balance Equatios in Finite-Volume Large-Eddy Simulations, Tech. rep., Department of Mechanical Engineering, Surrey University, England, 1994.

Geoffroy, O., Brenguier, J. L., and Burnet, F.: Parametric representation of the cloud droplet spectra for bulk microphysics, in preparation, 2009a.

Geoffroy, O., Brenguier, J. L., Burnet, F., and Siebesma, A. P.: Parametric representation of the rain droplet spectra for bulk microphysics, in preparation, 2009b.

Griffith, E. J., Post, F. H., and Heus, T.: A physically-correct GPU-accelerated, atmospheric large-eddy simulation, in: Eurographics/IEEE-VGTC Symposium on Visualization, rejected, 2009.

Haiden, T. and Whiteman, C. D.: Katabatic Flow Mechanisms on a Low-Angle Slope, Journal of Applied Metorology, 44, 113–126., doi:10.1175/JAM-2182.1, 2005.

Heus, T. and Jonker, H. J. J.: Subsiding shells around shallow

cumulus clouds, J. Atmos. Sci., 65, 1003–1018, doi:10.1175/2007JAS2322.1, 2008.

Heus, T., van Dijk, G., Jonker, H. J. J., and van den Akker, H. E. A.: Mixing in shallow cumulus clouds studied by Lagrangian particle tracking, J. Atmos. Sci., 65, 2581–2597, doi:10.1175/2008JAS2572.1, 2008.

Holtslag, B.: Preface: GEWEX Atmospheric Boundary-layer Study (GABLS) on Stable Boundary Layers, Bound.-Layer Meteor., 118, 243–246, doi:10.1007/s10546-005-9008-6, 2006.

Hundsdorfer, W., Koren, B., Vanloon, M., and Verwer, J. G.: A positive finite-difference advection scheme, J. Comput. Phys., 117, 35–46, doi:10.1006/jcph.1995.1042, 1995.

Jonker, H. J. J., Vilà-Guerau de Arellano, J., and Duynkerke, P. G.: Characteristic length scales of reactive species in a convective boundary layer, J. Atmos. Sci., 61, 41–56, doi:10.1175/1520-0469(2004)061⟨0041:CLSORS⟩2.0.CO;2, 2004.

Jonker, H. J. J., Heus, T., and Sullivan, P. P.: A refined view of vertical transport by cumulus convection, Geophys. Res. Lett., 35, L07 810, doi:10.1029/2007GL032606, 2008.

Joseph, J. H., Wiscombe, W. J., and Weinman, J. A.: The delta-Eddington approximation for radiative flux transfer, J. Atmos. Sci., 33, 2452–2459, doi:10.1175/1520-0469(1976)033⟨2452:TDEAFR⟩2.0.CO;2, 1976.

Kaimal, J. and Finnigan, J.: Atmospheric Boundary Layer Flows: Their Structure and Measurement, Oxford University Press, USA, 1994.

Khairoutdinov, M. and Kogan, Y.: A new cloud physics parameterization in a large-eddy simulation model of marine stratocumulus, Mon. Wea. Rev., 128, 229–243, doi:10.1175/1520-0493(2000)128⟨0229:ANCPPI⟩2.0.CO;2, 2000.

Khanna, S. and Brasseur, J. G.: Three-dimensional buoyancy and shear-induced local structure of the atmospheric boundary layer, J. Atmos. Sci., 55, 710–743, doi:10.1175/1520-0469(1998)055⟨0710:TDBASI⟩2.0.CO;2, 1998.

Kim, S. W., Park, S. U., Pino, D., and Vilà-Guerau de Arellano, J.: Parameterization of entrainment in a sheared convec boundary layer using a first-order jump model, J. Atmos. Sci., 120, 455–475, 2006.

Kosović, B. and Curry, J.: A Large Eddy Simulation Study of a Quasi-Steady, Stably Stratified Atmospheric Boundary Layer, J. Atmos. Sci., 57, 1052–1068, doi:10.1175/1520-0469(2000)057⟨1052:ALESSO⟩2.0.CO;2, 2000.

Krol, M. C., Molemaker, M. J., and Vilà-Guerau de Arellano, J.: Effects of turbulence and heterogeneous emissions on photochemically active species in the convective boundary layer, J. Geophys. Res., 105, 6871–6884, doi:10.1029/1999JD900958, 2000.

Larson, V. E., Kotenberg, K. E., and Wood, N. B.: An analytic longwave radiation formula for liquid layer clouds, Mon. Wea. Rev., 135, 689–699, doi:10.1175/MWR3315.1, 2007.

Lilly, D. K.: The representation of small-scale turbulence in numerical simulation experiments., in: Proc. IBM Scientific Computing symp. on Environmental Sciences, edited by Goldstine, H., pp. 195–210, 1967.

Louis, J. F.: A parametric model of vertical fluxes in the atmosphere, Bound.-Layer Meteor., 17, 187–202, doi:10.1007/BF00117978, 1979.

Neggers, R. A. J., Duynkerke, P. G., and Rodts, S. M. A.: Shallow cumulus convection: A validation of large-eddy simulation against aircraft and Landsat observations, Quart. J. Roy. Meteor. Soc., 129, 2671–2696, doi:10.1256/qj.02.93, 2003a.

Neggers, R. A. J., Jonker, H. J. J., and Siebesma, A. P.: Size statistics of cumulus cloud populations in large-eddy simulations, J. Atmos. Sci., 60, 1060–1074, doi:10.1175/1520-0469(2003)60⟨1060:SSOCCP⟩2.0.CO;2, 2003b.

Nieuwstadt, F. T. M. and Brost, R. A.: The decay of convective turbulence, J. Atmos. Sci., 43, 532–546, doi:10.1175/1520-0469(1986)043⟨0532:TDOCT⟩2.0.CO;2, 1986.

Nieuwstadt, F. T. M. and de Valk, J. P. J. M. M.: A Large eddy simulation of buoyant and non-buoyant plume dispersion in the atmospheric boundary layer, Atmos. Environ., 21, 2573–2587, doi:10.1016/0004-6981(87)90189-2, 1987.

Petersen, A. and Holtslag, A. A. M.: A first-order closure for covariances and fluxes of reactive species in the convective boundary layer, J. Appl. Meteor., 38, 1758–1776, doi:10.1175/1520-0450(1999)038⟨1758:AFOCFC⟩2.0.CO;2, 1999.

Petersen, A. C., Beets, C., van Dop, H., Duynkerke, P. G., and Siebesma, A. P.: Mass-flux characteristics of reactive scalars in the convective boundary layer, J. Atmos. Sci., 56, 37–56, doi:10.1175/1520-0469(1999)056⟨0037:MFCORS⟩2.0.CO;2, 1999.

Pincus, R. and Stevens, B.: Monte Carlo spectra integration: A consistent approximation for radiative transfer in large eddy simulations, J. Adv. Modeling Earth Sys., 2008.

Pino, D. and Vilà-Guerau de Arellano, J.: Effects of the shear in the convective boundary layer: Analysis of the turbulent kinetic energy budget, Acta Geophysica, 56, 167–193, doi:10.2478/s11600-007-0037-z, 2008.

Pino, D., Vilà-Guerau de Arellano, J., and Duynkerke, P. G.: The contribution of shear to the evolution of a convective boundary layer, J. Atmos. Sci., 60, 1913–1926, doi:10.1175/1520-0469(2003)060⟨1913:TCOSTT⟩2.0.CO;2, 2003.

Pino, D., Jonker, H. J. J., Vilà-Guerau de Arellano, J., and Dosio, A.: Role of the shear and inversion strength during sunset turbulence over land, Bound.-Layer Meteor., 121, 537–556, doi:10.1007/s10546-006-9080-6, 2006a.

Pino, D., Vilà-Guerau de Arellano, J., and Kim, S. W.: Representing sheared convective boundary layer by zeroth- and first-order jump mixed layer models: large-eddy simulation verification, J. Appl. Meteor., 45, 0000–0000, doi:10.1175/1520-0469(2003)060⟨1913:TCOSTT⟩2.0.CO;2, 2006b.

Randall, D.: Conditional instability of the fist kind upside down, J. Atmos. Sci., 37, 125–150, doi:10.1175/1520-0469(1980)037⟨0125:CIOTFK⟩2.0.CO;2, 1980.

Rauber, R. M., Stevens, B., Ochs, H. T., Knight, C. A., Albrecht, B. A., Blyth, A. M., Fairall, C. W., Jensen, J. B., Lasher-Trapp, S. G., Mayol-Bracero, O. L., Vali, G., Anderson, J. R., Baker, B. A., Bandy, A. R., F., B., Brenguier, J.-L., Brewer, W. A., Brown, P. R. A., Chuang, P., Cotton, W. R., Di Girolamo, L., Geerts, B., Gerber, H., Göke, S., Gomes, L., Heikes, B. G., Hudson, J. G., Kollias, P., P., L. R., Krueger, S., Lenschow, D. H., Nuijens, L., O'Sullican, D. W. O., Rilling, R. A., Rogers, D. C., Siebesma, A. P., Snodgrass, E., Stith, J. L., Thornton, D. C., Tucker, S., Twohy, C. H., and Zuidema, P.: Rain in (shallow) cumulus over the ocean - The RICO campaign, Bull. Amer. Meteor. Soc., 88, 1912–1928, doi:10.1175/BAMS-88-12-1912, 2007.

Rodts, S. M. A., Duynkerke, P. G., and Jonker, H. J. J.: Size distributions and dynamical properties of shallow cumulus clouds from aircraft observations and satellite data, J. Atmos. Sci., 60, 1895–1912, doi:10.1175/1520-0469(2003)060⟨1895:SDADPO⟩

2.0.CO;2, 2003.

Schumann, U.: Large-eddy simulation of turbulent diffusion with chemical reactions in the convective boundary layer, Atmos. Environ., 23, 1713–1729, doi:10.1016/0004-6981(89)90056-5, 1989.

Schumann, U.: Large-eddy simulation of the up-slope boundary layer, Quart. J. Roy. Meteorol. Soc, 116, 637–670, doi:10.1256/smsqj.49306, 1990.

Seifert, A.: On the parameterization of evaporation of raindrops as simulated by a one-dimensional rainshaft model, J. Atmos. Sci., 65, 3608–3619, doi:10.1175/2008JAS2586.1, 2008.

Seifert, A. and Beheng, K. D.: A double-moment parameterization for simulating autoconversion, accretion and selfcollection, Atmos. Res., 59, 265–281, doi:10.1016/S0169-8095(01)00126-0, 2001.

Seifert, A. and Beheng, K. D.: A two-moment cloud microphysics parameterization for mixed-phase clouds. Part 1: Model description, Meteor. Atmos. Phys., 92, 45–66, doi:10.1007/s00703-005-0112-4, 2006.

Shettle, E. P. and Weinman, J. A.: The transfer of solar irradiance through inhomogeneous turbid atmospheres evaluated by Eddingtons approximation, J. Atmos. Sci., 27, 1048–1055, doi:10.1175/1520-0469(1970)027⟨1048:TTOSIT⟩2.0.CO;2, 1970.

Siebesma, A. P. and Cuijpers, J. W. M.: Evaluation of parametric assumptions for shallow cumulus convection, J. Atmos. Sci., 52, 650–666, doi:10.1175/1520-0469(1995)052⟨0650:EOPAFS⟩2.0.CO;2, 1995.

Siebesma, A. P. and Jonker, H. J. J.: Anomalous scaling of cumulus cloud boundaries, Phys. Rev. Lett., 85, 214–217, doi:10.1103/PhysRevLett.85.214, 2000.

Siebesma, A. P., Bretherton, C. S., Brown, A., Chlond, A., Cuxart, J., Duynkerke, P. G., Jiang, H. L., Khairoutdinov, M., Lewellen, D., Moeng, C. H., Sanchez, E., Stevens, B., and Stevens, D. E.: A large eddy simulation intercomparison study of shallow cumulus convection, J. Atmos. Sci., 60, 1201–1219, doi:10.1175/1520-0469(2003)60⟨1201:ALESIS⟩2.0.CO;2, 2003.

Simpson, J. and Wiggert, V.: Models of precipitating cumulus towers, Mon. Wea. Rev., 97, 471–489, doi:10.1175/1520-0493(1969)097⟨0471:MOPCT⟩2.3.CO;2, 1969.

Sommeria, G.: Three-dimensional simulation of turbulent processes in an undisturbed trade-wind boundary layer, J. Atmos. Sci., 33, 216–241, doi:10.1175/1520-0469(1976)033⟨0216:TDSOTP⟩2.0.CO;2, 1976.

Sommeria, G. and Deardorff, J. W.: Subgrid-scale condensation in models of non-precipitating clouds, J. Atmos. Sci., 34, 344–355, doi:10.1175/1520-0469(1977)034⟨0344:SSCIMO⟩2.0.CO;2, 1977.

Stephens, G. L.: The parameterization of radiation for numerical weather prediction and climate models, Mon. Wea. Rev., 112, 826–867, doi:10.1175/1520-0493(1984)112⟨0826:TPORFN⟩2.0.CO;2, 1984.

Stevens, B., Ackerman, A. S., Albrecht, B. A., Brown, A. R., Chlond, A., Cuxart, J., Duynkerke, P. G., Lewellen, D. C., MacVean, M. K., Neggers, R. A. J., Sanchez, E., Siebesma, A. P., and Stevens, D. E.: Simulations of trade wind cumuli under a strong inversion, J. Atmos. Sci., 58, 1870–1891, doi:10.1175/1520-0469(2001)058⟨1870:SOTWCU⟩2.0.CO;2, 2001.

Stevens, B., Moeng, C. H., Ackerman, A. S., Bretherton, C. S., Chlond, A., De Roode, S., Edwards, J., Golaz, J. C., Jiang, H. L., Khairoutdinov, M., Kirkpatrick, M. P., Lewellen, D. C., Lock, A., Muller, F., Stevens, D. E., Whelan, E., and Zhu, P.: Evaluation of large-Eddy simulations via observations of nocturnal marine stratocumulus, Mon. Wea. Rev., 133, 1443–1462, doi:10.1175/MWR2930.1, 2005.

Stull, R. B.: An introduction to boudary layer meteorology, Kluwer Academic Publishers, 1988.

Sullivan, P. P., Moeng, C.-H., Stevens, B., Lenschow, D. H., and Mayor, S. D.: Structure of the entrainmentzone capping the convective atmospheric boundary layer, J. Atmos. Sci., 55, 3042–3064, doi:10.1175/1520-0469(1998)055⟨3042:SOTEZC⟩2.0.CO;2, 1998.

Thomson, D. J.: Criteria for the selection of stochastic models of particle trajectories in turbulent flows, J. Fluid Mech., 180, 529–556, doi:10.1017/S0022112087001940, 1987.

van Heerwaarden, C. C. and Vilà-Guerau de Arellano, J.: Relative humidity as an indicator for cloud formation over heterogeneous land surfaces, J. Atmos. Sci., 65, 3263–3277, doi:10.1175/2008JAS2591.1, 2008.

van Zanten, M. C. et al.: RICO Intercomparison, in preparation, 2009.

Verwer, J. G.: Gauss seidel iterations for stiff nodes from chemical kinetics, Journal of Scientific Computing, 15, 1243–1250, 1994.

Verwer, J. G. and Simpson, D.: Explicit methods for stiff ODEs from atmosperic chemistry, Applied Numerical Mathematics, 18, 413–430, doi:10.1016/0168-9274(95)00068-6, 1995.

Verzijlbergh, R. A., Jonker, H. J. J., Heus, T., and Vilà-Guerau de Arellano, J.: Turbulent dispersion in cloud-topped boundary layers, Atmos. Chem. Phys., 9, 1289–1302, http://www.atmos-chem-phys.net/9/1289/2009/, 2009.

Vilà-Guerau de Arellano, J. and Cuijpers, J. W. M.: The chemistry of a dry cloud: the effects of radiation and turbulence, J. Atmos. Sci., 57, 1573–1584, doi:10.1175/1520-0469(2000)057⟨1573:TCOADC⟩2.0.CO;2, 2000.

Vilà-Guerau de Arellano, J., Dosio, A., Vinuesa, J. F., Holtslag, A. A. M., and Galmarini, S.: The dispersion of chemically reactive species in the atmospheric boundary layer, Meteor. Atmos. Phys., 87, 23–38, doi:10.1007/s00703-003-0059-2, 2004.

Vilà-Guerau de Arellano, J., Kim, S. W., Barth, M. C., and Patton, E. G.: Transport and chemical transformations influenced by shallow cumulus over land, Atmos. Chem. Phys., 5, 3219–3231, 2005.

Vilà-Guerau de Arellano, J., van den Dries, K., and Pino, D.: On inferring isoprene emission surface flux from atmospheric boundary layer concentration measurements, Atmospheric Chemistry and Physics Discussion, 9, 4159–4193, 2009.

Vinuesa, J. F. and Vilà-Guerau de Arellano, J.: Fluxes and (co-)variances of reacting scalars in the convective boundary layer, Tellus B, 55, 935–949, doi:10.1046/j.1435-6935.2003.00073.x, 2003.

Vinuesa, J. F. and Vilà-Guerau de Arellano, J.: Introducing effective reaction rates to account for the inefficient mixing in the convective boundary layer, Atmos. Environ., 39, 445–461, doi:10.1016/j.atmosenv.2004.10.003, 2005.

Weil, J. C., Sullivan, P. P., and Moeng, C. H.: The use of large-eddy simulations in Lagrangian particle dispersion models, J. Atmos. Sci., 61, 2877–2887, doi:10.1175/JAS-3302.1, 2004.

Wesseling, P.: Von Neumann stability conditions for the convection-diffusion equation, IMA Journal of Numerical Analysis, 16,

583–598, doi:10.1093/imanum/16.4.583, 1996.

Wicker, L. J. and Skamarock, W. C.: Time-splitting methods for elastic models using forward time schemes, Mon. Wea. Rev., 130, 2088–2097, doi:10.1175/1520-0493(2002)130⟨2088:TSMFEM⟩2.0.CO;2, 2002.

Yaglom, A. M.: Comments on wind and temperature flux-profile relationships, Bound.-Layer Meteor., 11, 89–102, doi:10.1007/BF00221826, 1977.